Flame Temperature Imaging of a Low NOx Burner via Laser Rayleigh Scattering

Nicholas A. Smith
Marquette University

FLAME TEMPERATURE IMAGING OF A LOW NOx BURNER VIA LASER RAYLEIGH SCATTERING

by

Nicholas A. Smith, B.S.M.E.

A Thesis submitted to the Faculty of the Graduate School,
Marquette University,
in Partial Fulfillment of the Requirements for
the Degree of Master of Science

Milwaukee, Wisconsin

August 2013

ABSTRACT

FLAME TEMPERATURE IMAGING OF A LOW NOx BURNER
VIA LASER RAYLEIGH SCATTERING

Nicholas A. Smith, B.S.M.E.

Marquette University, 2013

Federal and global legislation are requiring increasingly stringent emission regulation on household appliances and in particular water heater burners. Emissions like NO_x (NO and NO_2) are a growing concern due to their adverse health effects and contribution to tropospheric ozone, acid rain, and smog formation. As NO_x is more closely controlled, appliance manufacturers are developing low emission burners for use in water heaters.

Flame temperature is strongly correlated to NO_x production. Hence, characterizing flame temperatures in new burners is a key part of improving upon burners used today and the development of future burners. Temperature measurements applied to a new, radiant, ultralow-NO_x burner are thus the focus of this research. Laser Rayleigh scattering allows us to make near-instantaneous, 2-D measurements using an unobtrusive technique. The application of this technique resulted in flame temperature images in three locations, above and across the burner surface ranging from 800-1600 K in general with an uncertainty of 9.6%. The fluctuation of the flame temperature was also found ranging from 200-800 K, indicating the presence of large scale hot and cold gas mixing.

Other temperature measuring techniques were applied to the burner as well. A type-K thermocouple 5 cm above the center of the burner measured a point gas temperature of 1508 K after an estimated radiative correction was applied. This measurement was within 5.3% of the laser Rayleigh scattering measurement of 1428 K at the same location. An IR camera did not provide quantitative temperature measurements, but the videos indicated similar flame structure and mixing behavior when compared to a series of single-shot laser Rayleigh scattering images.

It was concluded that the large amount of excess air (equivalence ratio of 0.725) was primarily responsible for reducing the flame temperature by 436 K in comparison with the adiabatic flame temperature under stoichiometric conditions. The radiative emission by the burner was estimated from the thermocouple and laser Rayleigh scattering measurements to decrease the temperature further by an average of 420 K relative to the stoichiometric adiabatic flame temperature.

ACKNOWLEDGEMENTS

Nicholas A. Smith, B.S.M.E.

I would first like to recognize Dr. Jon Koch for his guidance and support in this project. Dr. Koch has been the biggest influence on my academic career at Marquette University. His hard work greatly contributed to my achievements and significantly expanded my knowledge of engineering.

I would also like to acknowledge the advisement and support of my committee members, Dr. John Borg and Mr. David Kalensky. Both Dr. Borg and Mr. Kalensky have enhanced my education and helped in the preparation of this thesis. Furthermore, this project would not have been possible without the financial support of the Gas Technology Institute and their willingness to lend us an intensified camera and other system components.

I am very grateful to have had a Teaching Assistantship in the Department of Mechanical Engineering for the past 2 years and the numerous other opportunities that Marquette University has provided for me. I want to thank Annette Wolak for her assistance with all my questions and help on so many day-to-day issues. A special thanks to Hao Wang for his camaraderie and guidance in our graduate study.

Finally, neither this project nor my other endeavors would have been possible without the love and support of my friends (both near and far) and my whole family (mom, dad, and two brothers). Thank you all for supporting me.

TABLE OF CONTENTS

LIST OF TABLES

LIST OF FIGURES

LIST OF PRINCIPLE SYMBOLS

λ	wavelength
σ	Rayleigh scattering cross section
S	signal
x	mole fraction
I	laser pulse energy
Q	quantum efficiency
f	f number (lens)
t	percent transmission (lens)
r	index of refraction of molecule
n	number of molecules
B	background calibration matrix
B_{top}	blocked laser sheet image, section cut for B (also bottom and middle)
B_{avg}	average of B (single number), actual background used
$A_{1,2}$	air scattered signal (average of 1000 images for each 1 and 2)
$M_{1,2}$	background subtracted average air scattered signal
Z	flame scattered signal (average of 1000 images)
F	background subtracted average flame scattered signal
T_{RT}	room temperature
T_{Flame}	flame temperature
C	calibration constant matrix and quantum efficiency of optical system
h	enthalpy
Φ_{rad}	fraction of energy in radiation
$E_{rad,loss}$	energy leaving via radiation
$E_{adiabatic}$	amount of energy at adiabatic temperature
φ	equivalence ratio
δ	uncertainty operator
Ω	solid angle of receiving optics (small)
L	length of scattering volume
N	total number density
P	pressure
k	Boltzmann constant

CHAPTER 1

Introduction

1.1 Residential Water Heater Background

Water heater devices are a typical appliance found in almost all American homes. Among these, storage water heaters are the most commonly used. Storage water heaters operate by taking water from the cold water supply and heating it in a tank. The main sources of energy used to heat the water are natural gas and electricity. In natural gas storage water heaters, a thermostat controlled burner heats the water from below the tank, and as it warms, the water rises to the top of the tank to be distributed in the home. The American Housing Survey for the United States in 2009 states that 96 percent of all water heaters in use are gas or electric units, with a total of 60 million units being natural gas-fired storage water heaters with atmospheric burners [1]. According of the American Gas Association, water heaters consume the second greatest amount of energy in a home after the heating and cooling system [2]. In a 2010 overview of the water heater market by the U.S. Department of Energy, it was found that standard electric water heaters cost an average of $232 more per year to operate than a standard natural gas water heater due to the lower national average cost of natural gas [3]. Additionally, natural gas water heaters are capable of heating water twice as fast [2].

It has also been found that natural gas water heaters are more environmentally friendly than electric water heaters based on reported data about air pollutants and emissions. Because electricity is predominantly coal-based, electric water heaters produce 3 times more CO_2, 1000 times more SO_2, and 4 times more NO_x [4]. These combustion byproducts can have an effect on

our lives and the environment, and continuing efforts to control their excess production are a current research topic.

1.2 Background on Air Toxics from Combustion

In the 1970s and 80s non-methane volatile organic compounds (NMVOC) and air toxics (such as benzene, dioxins, inorganic *HCl*, metal oxides and chlorides, and aerosol particles less than 10 μm) were a growing concern as their adverse health effects and contribution to ozone formation were realized. Particularly relevant to this study is the formation of NO_x. Nitrogen oxides (NO_x) refer specifically to the molecules *NO* and NO_2, which are stable when isolated, but can also be quite reactive in high temperature environments. Nitrogen oxides are a product of combustion and are released into the atmosphere where they are one of the main contributors to smog and the formation of tropospheric (ground-level) ozone, as well as precursors to acid rain.

In the past century, nitrogen oxide (as well as many other) emissions from the combustion of fossil fuels have risen on a global scale. In the United States, the Clean Air Act has been a major milestone in the control of air pollution. The Clean Air Act of 1963 was the first federal program to address the control of air pollution [5]. The Clean Air Act was expanded in 1970 to implement new federal and state emission controls of both industrial and mobile/automotive sources of air pollution, as well as impose greater enforcement of these policies [5]. The act set the current standard of 53 ppb for nitrogen dioxide (NO_2) concentrations, the most prevalent form of NO_x [6]. In the 1990s, concerns about acid deposition (acid rain) control caused mainly by NO_x and SO_2 were legislated into emission reduction and control mandates in combustion processes and have been the last major revision to the original Clean Air Act to date [7]. In the past 20 years in particular, NO_x emissions

regulations alone have become more strict, especially in developed countries on smaller combustion devices [8]. While previous control regulations by the Environmental Protection Agency (EPA) have been directed toward large-scale plants, industrial emission sources, and mobile (automobiles) applications, smaller combustion applications and devices are of increased interest due to the millions of units operating in the United States and their relatively higher NO_x emission. In the past 30 years with higher emission control, NO_2 concentrations have decreased by more than 40% to today's concentrations of 10-20 ppb [6].

Optimizing combustion processes and controlling air toxics emission is an essential task in the present day, not only due to stricter new legislation and policies, but also for our health and the environment. Progress in the control of SO_2 in fossil fuel power plants, for example, has been significant with the implementation of flue-gas desulfurization (FGD) systems to reduce the amount of SO_2 released into the atmosphere with removal efficiencies of 50-98 % [9]. Despite advances in the control of certain emissions in large scale plant environments, other molecules like NO_x still present an emission control challenge in small scale applications like water heater burners and require further research to cost-effectively reduce their levels.

1.3 Low NOx Water Heater Burner Background

As discussed previously, millions of water heater systems in the United States utilize a natural gas fired, partially premixed fuel and air burner to heat water for use in the home. The amount of NO_x produced by these burners varies by application and amount of technology implemented on a specific system, but low-emission water heater burners (LEWHB) are increasingly desirable so that emissions meet new stricter standards set by the EPA. Manufacturers and researchers have developed several approaches to implement low-emission

water heater burners to achieve the limit of 10 ng/J for NO_x [10]. This current ultra-low NO_x emission limit of 10 ng/J (15 ppmv NO_x at 3% O_2) is set by a number of new laws like the South Coast Air Quality Management District (SCAQMD) Rule 1121 which pertains specifically to water heaters sold after July 2007 and under 75,000 Btu per hour [11]. These new regulations are part of a federal EPA State Implementation Plan (SIP) that outlines how states can attain and uphold National Ambient Air Quality Standards (NAAQS) set by the Clean Air Act which covers a wide-range of species in the atmosphere.

The central objective then for new low-emission water heater burners is to reduce the total NO_x formation. The total of NO_x in combustion can be broken into thermal, fuel, and prompt NO_x, where thermal is often the most significant in natural gas combustion. Since thermal NO_x depends greatly on combustion temperatures, reducing the flame or combustion temperature can significantly minimize the total NO_x formation [12]. In fact, the EPA's first method for NO_x abatement and control lists the reduction of combustion temperatures as a successful technology [13]. Several methods have been developed to reduce NO_x formation in water heater burners. One approach that has been developed for commercial gas water heaters is the addition of a flue gas recirculation (FGR) system [14]. The flue gas recirculation system directs the flue gases from combustion back into the burner inlet where these gases can then absorb heat and therefore lower peak flame temperatures. The flue gas also lowers the average oxygen content, which then depletes one of the necessary molecules for NO_x formation [15]. While flue gas recirculation can reduce emissions, these systems are more expensive and require additional electricity for operation. Furthermore, the addition of the flue gas to the burner inlet's flow can reduce the heating capacity of the water heater and result in some instabilities that would not otherwise be present [10]. An emission reduction method that is cost effective, highly

adaptable to current residential water heater systems and burners, and one that does not require additional energy input is still desirable.

The burner used for this study is a Beckett low-NO_x burner (40,000 Btu/hr) with a horizontal fuel jet that entrains air before flowing into a rectangular combustion cavity. The combustion gases then exit through a horizontal, planar metal wire mesh. In operation, the flame height is reduced and fluctuates close to the mesh. Since this burner is not yet well studied, any 2-D temperature measurements of the combustion gases using a laser spectroscopic technique are novel. The burner is shown and discussed further in *Burner System*.

1.4 Temperature Measurement Using a Thermocouple

With the main focus of this study being temperature measurement of the burner flame, a measurement technique needs to be selected. One approach to measuring flame temperature might be the use of a thermocouple. In using this technique however, many challenges arise. Inserting a thermocouple into a combustion process can modify the structure and behavior of the flame of interest. Physical probes also offer limited spatial resolution and time response. Accurate readings on a thermocouple require time for the temperature to stabilize and while this time could be relatively small, an unstable flame presents a fixed probe with a fluctuation temperature.

Furthermore, a physical device has challenges when faced with high-speed flows, high temperatures, pressures, or an environment with soot production, for example. Thermocouples also require a correction for radiation, convection, and conduction since this device measures its own temperature and not the gas temperature directly [16]. Keeping in mind thermocouples are point measurements, they would require multiple experiments in order to map a spatial profile of a flame temperature, whereas many laser techniques can provide nearly instantaneous 2-D

measurements. One study compared an identical flame experiment done with natural gas where thermocouple readings were compared to a CARS laser technique and found that there was a 300 K difference in the temperature measurements [17]. Despite often straight-forward temperature measurements using thermocouples in a wide range of applications, thermocouples reach severe limitations in high temperature and combustion applications. Laser techniques have therefore become popular and attractive in these research environments.

1.5 Temperature Measurement Using Laser Diagnostics

Almost all the disadvantages associated with thermocouples and mechanical measurement devices are inapplicable to laser probing techniques. Lasers offer unobtrusive measurements with high spatial (< 1 mm^3) and temporal (< 10 nsec) resolution, which are dependent on the amount of signal that can be obtained in a given experiment [18]. Laser techniques are particularly attractive for measurements taken in combustion zones, recirculation zones, and boundary layers where the flow is turbulent. Since these techniques are nonintrusive, there is also theoretically no upper bound to temperature measurements due to the absence of any physical device [16].

Despite numerous advantages in laser diagnostics, challenges also exist with these techniques. The most limiting factor can often be the requirement for optical access to the testing area. This requires a window to the field of interest, for example in a piston cylinder device or gas turbine. Laser diagnostics are also unable to measure all of the species and their respective temperatures in an area of interest at the same time. In order to fully analyze a situation, multiple approaches are taken, such as Rayleigh scattering, spontaneous Raman scattering, laser-induced fluorescence (LIF), and coherent anti-stokes Raman scattering (CARS)

which are further discussed below in *Review of Temperature Measurement by Laser-Spectroscopic Techniques in Flames.*

Additionally, laser spectroscopy is best utilized for small molecules (< six atoms). Larger molecules present more complicated analysis [16]. Since laser diagnostics do not offer a single technique in temperature measurement of combustion flows, a specific technique needs to be carefully determined in order to produce the most accurate desired measurements. This is often due to, for example, soot formation, pressure variations, and turbulent versus laminar flows [19]. Lastly, laser techniques require a high level of user knowledge and skill. While many people can buy the equipment and tools to set up a measurement experiment, there currently are few industry tools for commercial use in species and temperature measurements that can be easily adaptable. These laser tools are also relatively expensive in practice [16].

1.6 Review of Temperature Measurement by Laser-Spectroscopic Techniques in Flames

In general there are two approaches to temperature measurements using laser-spectroscopic techniques. First, a total number density measurement of the combustion gases can be related to the temperature using, for example the ideal gas law. This assumes a constant pressure condition. Secondly, temperature can be found using the internal energy modes of molecules by measurements of their population distribution in rotation or vibration [19].

1.6.1 Rayleigh Scattering

Rayleigh scattering is the elastic scattering of photons from gas molecules. An incoming photon causes a molecule to enter a ground-state vibrational mode, which results in emission of light in all directions at the incident photon's frequency and wavelength since there is no energy exchange [20]. This phenomenon can be used to explain why the sky is blue. Blue light is

strongly scattering laterally from the sky by the large amount of nitrogen and some oxygen molecules. Sunsets are then rich in orange and red, which are further down the spectrum due to the point-of-view of the observer. In this case, there is a greater volume of atmospheric air and more unscattered red and orange light is noticeable to the eye.

So, Rayleigh scattering can then be a useful spectroscopic tool since photon emission is nearly identical to incident light [16]. However, in the blue sky example, scattering is species specific and the sky might be a different color if the atmosphere was filled with molecules other than nitrogen and oxygen. Rayleigh scattering can be useful in the study of complex gas flows, and particularly the combustion of natural gas. Temperature and density are commonly determined using this technique [21]. The imaging technique is discussed further later in *Temperature Measurement via Rayleigh Imaging*.

1.6.2 Spontaneous Raman Scattering

Spontaneous Raman scattering differs from Rayleigh scattering because it is the inelastic scattering of photons. In this case there is some energy exchange and the wavelength of the incident photon is then shifted when the photon is scattered. The amount of energy that is exchanged in this process (and the corresponding shift in photon wavelength) depends on the polarization of the excitation source as well as the rotational and vibrational characteristics of the molecule. This approach produces approximately 0.1% of the signal in comparison with Rayleigh scattering, so the best results are usually obtained with steady, laminar flames where point or line measurements can be taken over a period of time [19]. For these reasons, spontaneous Raman scattering was not employed in this experiment.

1.6.3 Laser-Induced Fluorescence (LIF)

Laser-Induced fluorescence is unlike Rayleigh and Raman scattering in that it is a resonant process of photon absorption followed by spontaneous emission. LIF is also specific to a molecular species, which dictates a specific incident wavelength. This means in order for absorption and emission to occur, the incident light must be at the specific wavelength or energy for the molecule being probed. Thus, a pulsed, tunable laser is required for LIF experiments. Cost and availability of these lasers can limit the applications of LIF, whereas Rayleigh and Raman scattering can be performed with a large range of laser wavelengths.

Cross sections for the absorption and emission process when compared to molecular scattering are about ten orders of magnitude larger in LIF [19]. Due to this strong signal for specific molecules, LIF is quite useful in 2-D thermometry applications and can be more practical in combustion where there is an abundance of spurious scattered light, a problem for Rayleigh thermometry [19]. While LIF has many advantages in thermometry, it is limited by a single species temperature measurement and a tunable laser was not available for this study. For these reasons LIF was not utilized in this experiment.

1.6.4 Coherent Anti-Stokes Raman Scattering (CARS)

Similar to Raman scattering, CARS uses the same molecular transition but with signal amplification processes. CARS is the most developed coherent technique in combustion temperature measurement. Coherent techniques typically require high standards on laser beam stability, quality, and alignment. Since this is a nonlinear method, there is greater computational effort required in the determination of temperature [19]. However, this technique does offer probing capabilities in a luminous flame even when particulates exist in the region of interest.

Additionally, CARS can produce signals which are orders of magnitude greater than spontaneous Raman scattering [16]. As in the spontaneous Raman scattering technique, CARS is specific to a single species. Species independent 2-D temperature measurement is desired for this study, which CARS cannot achieve.

1.7 Temperature Measurement via Rayleigh Imaging

In this study, Rayleigh scattering was selected for a flame temperature measurement. The challenges and benefits are discussed further. Experimentally, this approach is quite attractive due to its relatively straightforward experimental set-up, high signal strength on a molecular level, and capability to provide near-instantaneous measurements in 2-D. This approach produces the best results usually with free burning, low luminosity flames that have few particulates. Spurious scattered light is also an important consideration and background scatter needs to be minimized [19]. Initial testing in ambient air contained Mie scattering from dust particulates which presented significant noise in preliminary images.

As discussed in *Rayleigh Scattering,* this technique utilizes the elastic scattering of photons in gas molecules. The Rayleigh signal is given in Equation 1.1 and can be considered as the amount of photons collected by the camera optics that are converted into an electrical signal by the detector at each pixel.

$$S_{Ray} = CI_o N \frac{d\sigma_{eff}}{d\Omega} \Omega L \tag{1.1}$$

C is the quantum efficiency of the optical system and detector (CCD camera), I_o is the incident laser energy, N is the total number density, $\frac{d\sigma_{eff}}{d\Omega}$ is the differential Rayleigh scattering cross section, Ω is the (small) solid angle covered by the collection optics, and L is the length of

scattering volume. In this experiment, the gas is a mixture so Rayleigh signal is equal to the weighted mole fraction average of the individual molecules given by Equation 1.2 [19].

$$\sigma_{eff} = \sum_{i=1}^{j} x_i \sigma_i \tag{1.2}$$

In this study, the mole fractions were determined using the products of combustion of methane (CH_4) and air ($O_2 + N_2$) $\rightarrow CO_2$, H_2O, N_2, and O_2.

In order to determine the temperature of the gas, *T*, two images need to be taken. One image is taken at STP and another of the combustion process. The temperature of the gas, *T*, was found using Equation 1.3.

$$\frac{T}{T_{ref}} = \frac{\sigma_{eff}}{\sigma_{ref}} \frac{S_{ref}}{S_{Ray}} \tag{1.3}$$

The reference state is defined to be at standard temperature and pressure and σ_{ref} is the effective cross section of the ambient air. Using this definition, we can determine the temperature of the gas molecules in the combustion process [3].

CHAPTER 2

Experimental Apparatus and Design

2.1 Rayleigh Scattering Experimental Apparatus Overview

The experimental setup for this study consists of many elements as outlined in the following pages. The main components are an EKSPLA pulsed Nd: YAG laser (NL303D - class IV), The Cooke Corporation, dicam pro, intensified CCD camera, and a low-NO_x water heater burner (40,000 Btu/hr) from Beckett. In overview, the laser is pulsed then shaped and steered by various optical components until it reaches the region above the burner in the form of a planar sheet and into the beam catch. The scattering of the laser photons by the gas molecules are collected when the laser is pulsed by the CCD camera. A top view of the experimental apparatus is shown in Figure 2.1. The purpose and placement of the beam blocking points shown in red will be discussed in detail in *Background Calibration*.

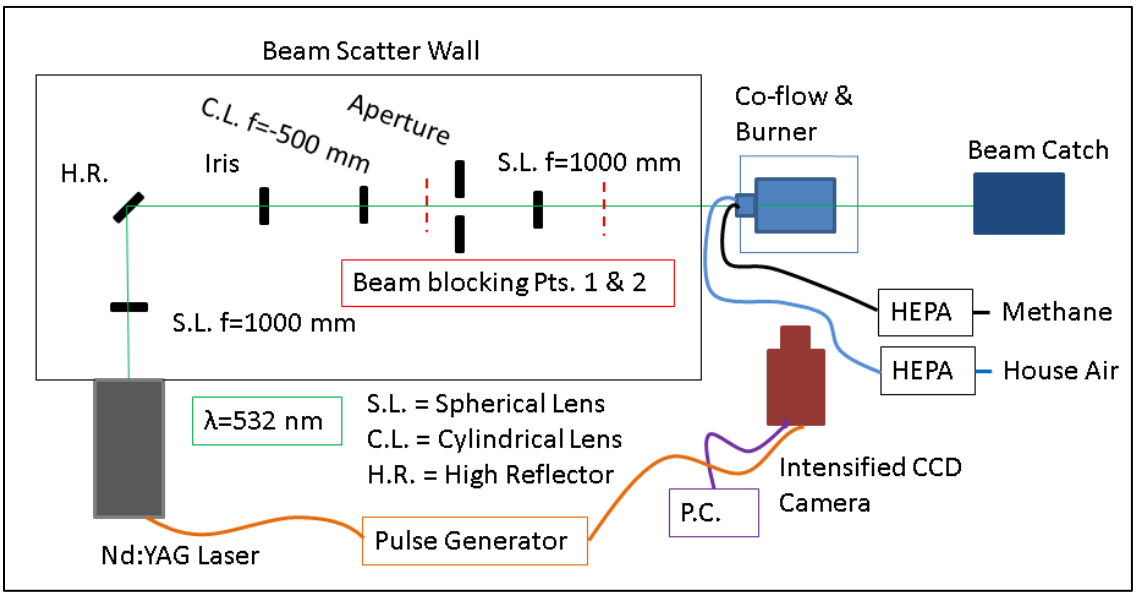

Figure 2.1: Top View of Entire System

2.2 Selection of Laser Wavelength

The first consideration of the system design was the selection of the laser wavelength to be used in the experiments. The laser, a pulsed Nd: YAG laser, available for this study has 4 available wavelengths it is capable of producing. The fundamental output wavelength of 1064 nm (infrared) can be frequency-doubled to the second harmonic, 532 nm which is half the fundamental wavelength and the most common example for Nd: YAG lasers [22]. In a similar manner, 355 nm and 266 nm are obtained. Three of the four available wavelengths were considered for the experiment. The standard wavelength of 1064 nm was not a consideration since it is in the infrared spectrum and no camera or lens for this wavelength was available for this study.

To begin the selection, the governing chemical reaction assuming major products was considered (Equation 2.1).

$$CH_4 + \frac{2}{\varphi}(O_2 + 3.76N_2) \rightarrow CO_2 + 2H_2O + \frac{7.52}{\varphi}N_2 + (\frac{2}{\varphi} - 2)O_2 \tag{2.1}$$

As shown, the governing reaction is methane and air with φ as the equivalence ratio. Since a typical water heater burner is used with natural gas and air, we can model the actual reaction with methane and air. The equivalence ratio (φ) for this study was set to 0.725 based on water heater manufacturer data, or 38% excess air – fuel lean combustion.

The Rayleigh cross section in air was determined for each of the products (CO_2, H_2O, N_2, O_2) by Equation 2.2. The cross section represents the area of the molecule that interacts with the incoming electromagnetic radiation and results in scattered light.

$$\sigma_{product} = \frac{4\pi^2 (r_{product} - 1)^2}{n^2 \lambda^4} \tag{2.2}$$

In Equation 2.2, *r* is the index of refraction of the molecule at a specific wavelength, λ is the wavelength, and n is the number density of molecules. The number density, *n*, is given by Equation 2.3 (the ideal gas law) at STP.

$$n = \frac{P}{kT} \tag{2.3}$$

By classical definition, *P* is pressure, *T* is temperature and *k* is the Boltzmann constant. From this, the effective Rayleigh cross section can be found from Equation 1.2 which will ultimately determine the amount of signal that can ideally be collected (Equation 2.4).

$$\sigma_{eff} = \sigma_{CO_2} x_{CO_2} + \sigma_{O_2} x_{O_2} + \sigma_{N_2} x_{N_2} + \sigma_{H_2O} x_{H_2O} \tag{2.4}$$

The mole fraction of each molecule is defined as *x*. The Rayleigh signal is then proportional to the variables in Equation 2.5 for the 3 wavelengths in question. It stems directly from Equation 1.1.

$$S_\lambda \propto I_o \sigma_{eff} Q_E \lambda \frac{1}{f^2} t \tag{2.5}$$

I_o is the laser pulse energy for the respective wavelength, Q_E is the quantum efficiency of the camera's photocathode and intensifier at a given wavelength, *f* is the f-number of the UV/Visible lens available, and *t* is the percent transmission of each lens. The values used in the following signal calculation are listed in Table 2.1.

Table 2.1: Signal Calculation Variable Values

Wavelength (λ) [nm]	I_o[J]	Q_E	f	t
532 (Nikon Lens)	720 x 10^{-3}	0.10	3.5	0.95
355 (UV Lens)	380 x 10^{-3}	0.17	1.2	0.85
266 (UV Lens)	160 x 10^{-3}	0.20	1.2	0.87

The actual signal is related to these variables by a proportionality constant which was omitted in the calculation since the constant includes parameters that are not easily determined, but also because they are constant for all three wavelengths in question (no change in experimental setup). The factors not included in this calculation are: Ω - the solid angle of camera optics, N - number density, C – other inefficiencies in the optical system, and L - length of scattering volume. The proportional signal is then determined. The results of Equation 2.4 and 2.5 are shown in Table 2.2.

Table 2.2: Wavelength Selection Results

Wavelength (λ) [nm]	Effective Cross Section [m^2]	Signal [J]
532 (Visible-Green)	7.31 x 10^{-32}	1.85 x 10^{-39}
355 (UV)	3.97 x 10^{-31}	6.31 x 10^{-40}
266 (UV)	1.33 x 10^{-30}	1.08 x 10^{-39}

From this analysis, it was concluded that a wavelength of *532 nm* provided the largest signal for the study with the available equipment and resources.

2.3 Laser and Optical System

The laser is pulsed with a Q-switch delay of 400μs and wavelength of 532 nm. The selection of this wavelength is discussed in detail in the previous section. The laser beam is first directed to the burner via a plano-convex spherical lens (f =1000 mm), high reflector then through an iris. This redirection of the beam, rather than the laser having a direct line of sight with the burner, is designed to keep excess scattering away from the imaging region down field. The beam is then shaped into a vertical sheet of height 9.6 cm and a width of 1 mm at the burner

imaging location via a plano-concave cylindrical lens (f = -500 mm) and a plano-convex spherical lens (f =1000 mm). The distance between the plano-convex spherical lens and the burner imaging point is approximately 152 cm. All lenses are antireflection coated. An aperture is also used down field of these two lenses to block any undesired divergence from the lens. The beam region from the opening of the laser until the last aperture is walled on all sides and top by either black felt or poster board painted matte black, with a rectangular slot for the laser sheet to exit to the burner region. Especially with a combination of lens and reflectors, there can be significant undesired scattering of laser light in many directions. These "beam scatter walls" control the scattering. After the laser sheet passes over the burner, it is contained in a rectangular box covered in black felt on the interior. The front of the box is also cover in felt with only a narrow slit for the laser sheet to pass through. This is done, again, to keep excess scattering away from the burner and imaging system.

2.4 Imaging System

The camera is mounted to the table and uses a Nikon Nikkor 50 mm lens (1:1.2, 389221) in conjunction with 2 close up lenses (+1 and +2 Hoya). A bandpass filter is also used with this camera so it only captures light from the laser wavelength (532 nm) with a 1 inch lens hood. The laser and camera are synced so that the camera gate is open when the laser pulses. This was observed and set using an oscilloscope (Tektronix Digital Phosphor, DPO 4032), light detector (Thor Labs Si Based, DET10A), and a BNC pulse/delay generator (model 565). In these measurements, the camera gate time was set to 200 ns. For each measurement, 2 by 2 pixel hardware binning was implemented to reduce read-out noise. The camera is also linked to a PC for data acquisition.

Additionally, the camera lens plane was parallel to the laser sheet which passes over the burner. This distance was set to 31.1 cm. Beyond the laser sheet, a plain black felt sheet was mounted vertically to provide a uniform background for the camera. See Figure 2.2 for a photo of this system with the camera, burner and co-flow. The honeycomb inserts are discussed further in *Co-flow System*.

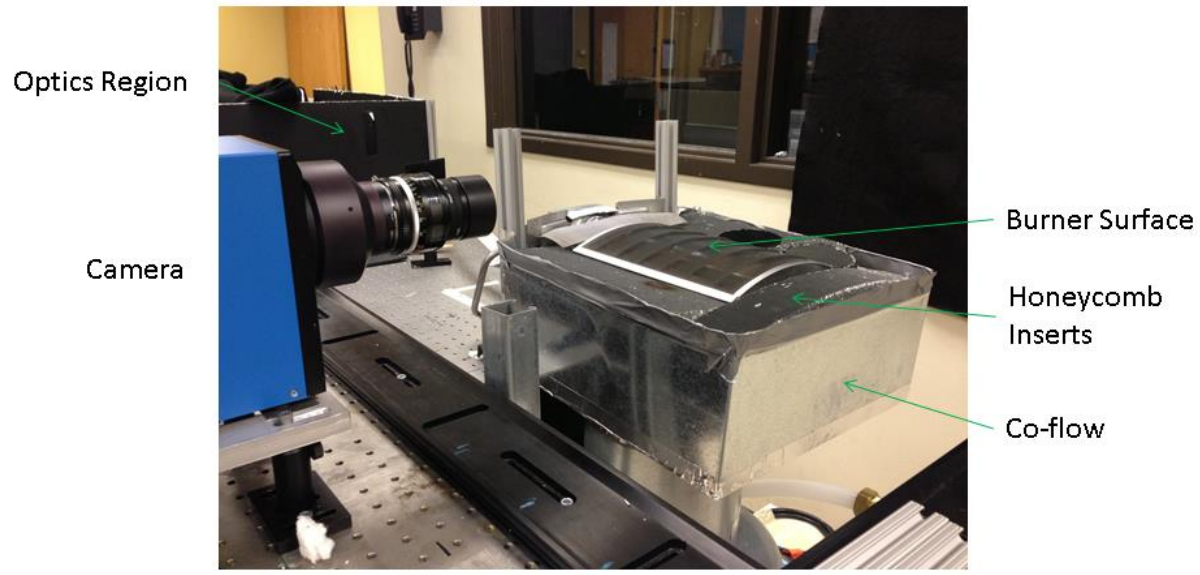

Figure 2.2: Camera, Burner and Co-flow Setup

2.5 Burner System

The burner (10 x 7.5 x 2.5 in) is supplied by two lines (air and fuel). Methane (industrial grade) was selected since it is approximately 90% of the composition of natural gas, the intended fuel for this burner. The fuel line originates from an industrial methane tank and controlled by the pressure regulator (Pro Star PRX 21213) and mass flow controller (FMA 5426), which is controlled by a transistorized power supply (Heath EUW-17) and multimeter (Omega Omegaette HHM93). A home-made fuel filter is used to prevent large particles from entering the burner flow. This consists of a 2 inch steel pipe with screw caps at the ends. Fittings are at each end for

the flow to enter and exit. A cylindrical vacuum-style HEPA air filter is contained inside to ensure fuel purity and arrest large particles.

The air-line is supplied by the house compressed air and is filtered by a modified HEPA filter system. The body of the system is based on a home filtration unit (Fantech Home HEPA filtration unit, DM 3000P), which is sealed on all sides (RTV Silicone) for this use along with an entrance and exit fitting. The exit side includes an external flow meter (Dwyer 600 SCFH) to monitor the flow rate for the burner inlet. This air HEPA filtration system is critical to the experiment as the house air supply contains many large particles and would present significant noise in a Rayleigh scattering signal otherwise.

The burner's inlet has also been modified so only the filtered air and fuel with known flow rates enter the burner for combustion. A 2 by 3 inch aluminum block was sealed to the inlet with fittings for a fuel inlet in-line with the burner at the same distance it is normally mounted, and 2 air lines which are split from the supply line that are in the same plane as the fuel inlet. This is to encourage a well-mixed flow to the burner, as in normal operating conditions. See Figure 2.3 for a photo of this modification.

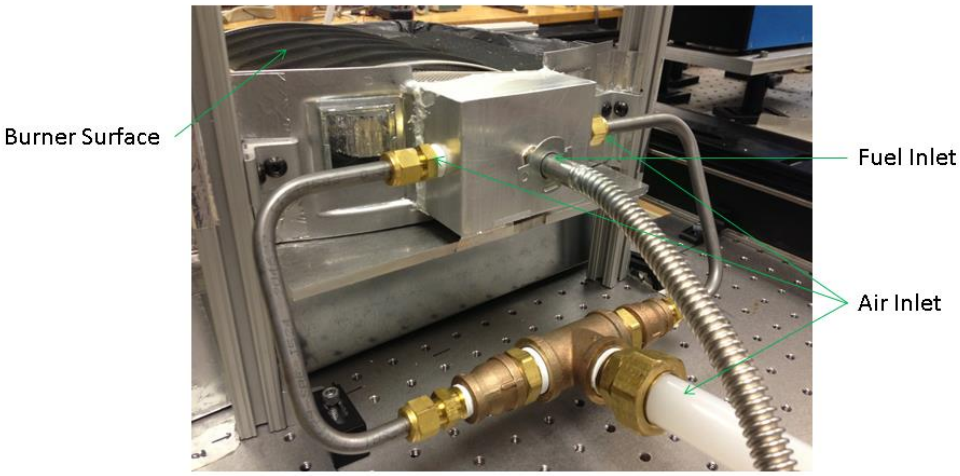

Figure 2.3: Burner Air and Fuel Inlet Modification

In normal operation, the flow rate for each line was set to a constant for all tests to ensure consistency and results for a very similar system that is in a typical home. The air flow rate was set to 16450 L/hr and the fuel flow rate was 1250 L/hr. These flow rates result in a firing rate of 39,067 Btu/hr with 38% excess air.

2.6 Co-flow System

The co-flow system was also introduced in order to provide the burner with HEPA filtered room temperature air flowing upwards (low rate) on all of the outer sides to obtain a Rayleigh signal free of Mie scattering (large dust particles) upon entrainment when the burner is in operation. A fan (Tjernlund M-8), controlled by a variac (Staco 3PN501) at 30% maximum voltage, supplies a sheet metal duct with air flow. The outlet is 14 by 14 inches with a standard home air filter, immediately followed by a HEPA filter that is approximately 3 inches below the bottom of the burner. Additional pieces of honeycomb are added as needed to the spaces between the edge of the burner and the metal duct outlet. Figure 2.2 shows an actual photo of this concept. A side profile sketch of this system is show in Figure 2.4.

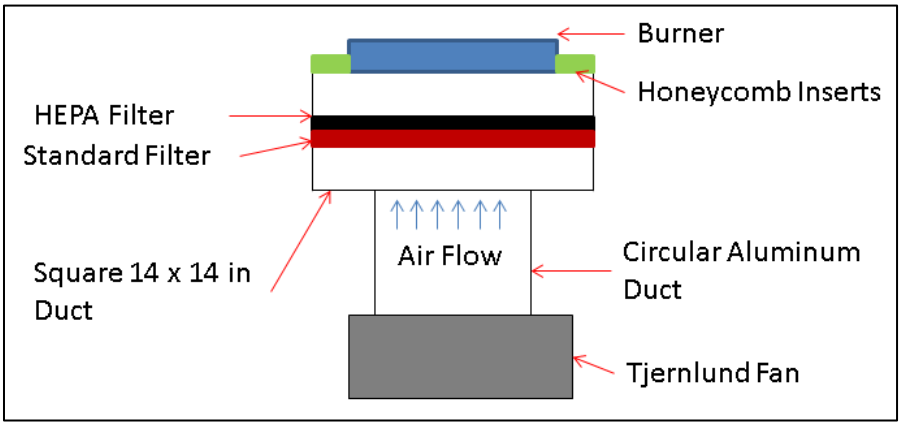

Figure 2.4: Co-flow System Sketch (Side Profile)

2.7 Thermocouple Measurement and IR Camera Experimental Setup

In addition to the Rayleigh scattering experiment that is the main focus of this study, temperature measurement by a thermocouple and IR camera were also performed for comparison. The thermocouple used was a Type-K (chromel alumel) probe-style device which was interfaced with LabVIEW software for temperature calculation. A maximum temperature measurement of 1372°C or 1645 K was limited by this thermocouple type in LabVIEW.

The burner remains in the same position as in the Rayleigh scattering experiment and remains operating at the normal conditions and flow rates. The co-flow system is removed, however since the thermocouple isn't affected by the presence of small dust particles. The thermocouple probe is held horizontally, with the tip reaching the center of the burner. The thermocouple is then connected to the computer and LabVIEW interface via a BNC analog connector box (NI BNC-2110) and data acquisition card. An image of the measurement setup is shown in Figure 2.5, where the tip of the probe is 5 cm from the surface of the mesh on the burner and positioned centrally.

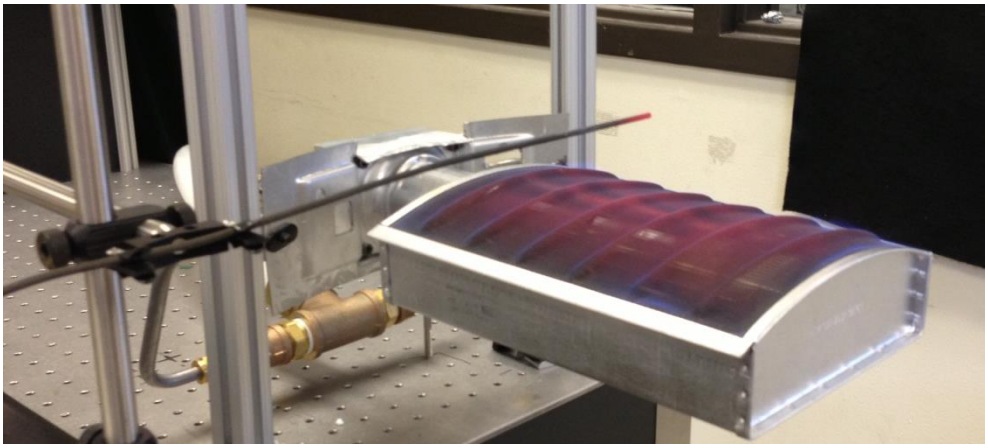

Figure 2.5: Thermocouple Measurement Setup

An infrared camera was then used to further explore the burner and flame temperature. A FLIR (E49001) thermal imaging camera was used for image collection. The temperature range of this particular model was -4 to 1202°F or 253 to 923 K. Again, the burner remains in the same position as in the Rayleigh scattering experiment and at the normal operating conditions and flow rates without the co-flow in place. The infrared camera was positioned on a tripod with the imaging field of view just above the burner surface, capturing the lower flame structure. The camera lens was placed 52 cm from the centerline of the burner.

CHAPTER 3

Imaging and Post-Processing

3.1 Overview

With the experimental apparatus now detailed, the temperature imaging and post-processing can now be described. In order to gain a deeper understanding of this burner, 3 imaging locations were selected. Figure 3.1 shows the imaging locations where the temperature is ultimately determined.

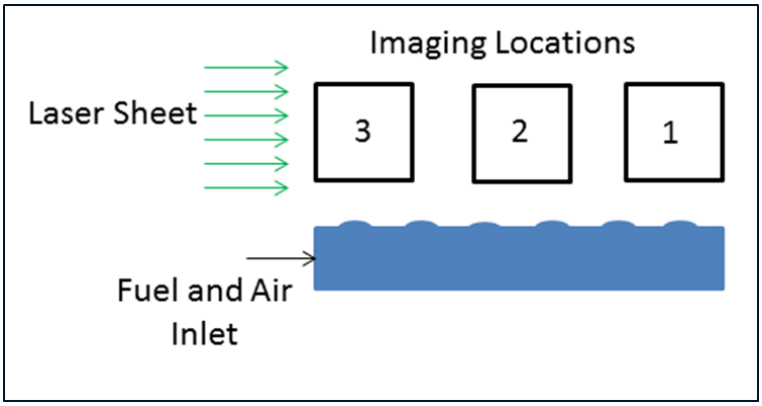

Figure 3.1: Imaging Locations

At each location, a series of images were collected. First, a spatial calibration image was taken, followed by 3 background images using a blocking technique. The 3 blocked regions of the images are stitched together to create a background image. Then, two large sets of images were collected for a case with only filtered air in the field of view and a case with the burner flame in its standard operation. With the background subtracted from the air and burner image sets, the flame temperature can then be found by relating the air images to a constant, room temperature value. A calibration matrix can then be defined to find the actual flame temperature,

relating the room temperature air and burner flame images. Each step of the image collection process and post-processing is discussed in further detail in the following sections. Imaging Location 1 is used to detail the imaging and post-processing in the following sections. Matlab source code used in the processing of these images and temperature is found in *APPENDIX III*.

3.2 Spatial Calibration

A spatial calibration technique is used to ensure an image is in focus and the size of the imaging window can be determined. In this study, a business card was used as the spatial calibration. The relative postion of the business card, as well as the imaging window is noted in Figure 3.2.

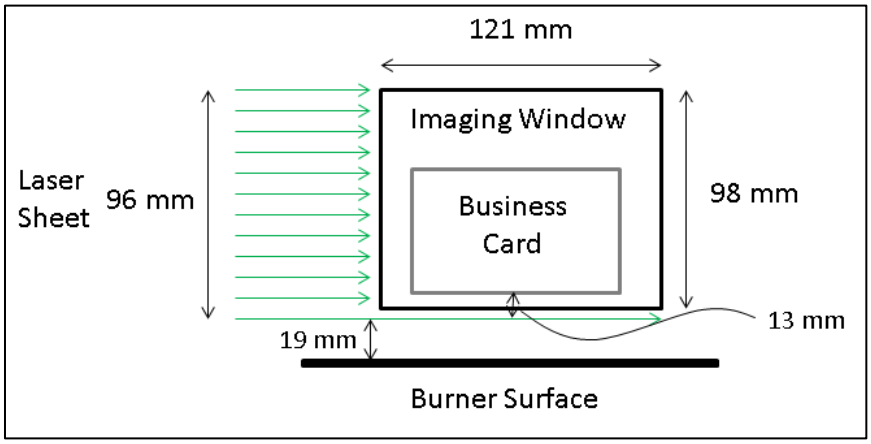

Figure 3.2: Relative Position of Imaging Window

The size of the imaging window was found by using the standard business card size and the number of pixels (512 rows x 640 columns – 16 bit .asc image). So, the length of each side of the card is related to the number of pixels along that distance.

3.3 Background Calibration

Determining the background signal is an important step in imaging measurement systems. This background will account for ambient condition signal and any spatial bias in the image. The technique used in this study, which was previously mentioned in *Temperature Measurement via Rayleigh Imaging*, is a technique previously employed by Su et al. [23]. Figure 3.3 illustrates the beam blocking technique in detail. Note the beam block points are approximately 45 cm separated and the laser sheet is much smaller in height since the sheet is blocked just after the cylindrical lens where the beam is still diverging. Therefore, the 1 cm block can cover approximately a third of the total sheet at that point.

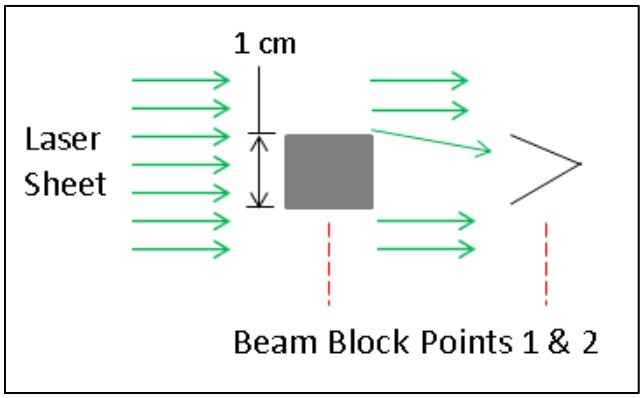

Figure 3.3: Background Blocking Method

Since taking background images with the laser off or blocked before the measurement field results in a background signal that doesn't account for laser scattering in the measurement field, the laser is allowed to propagate through the measurement field for background signal measurements. A beam block is then implemented, which is a fraction of the laser sheet profile. In this experiment the beam block was 1 cm. By imaging part of the laser sheet with a fraction blocked before the measurement field, a more accurate background signal is obtained in that

blocked region since most of the laser sheet is in view. Patching multiple averaged images together when the laser sheet is blocked across its entire length produces a background image for subtraction from raw signal images. The process of creating the background image in shown in Figure 3.4.

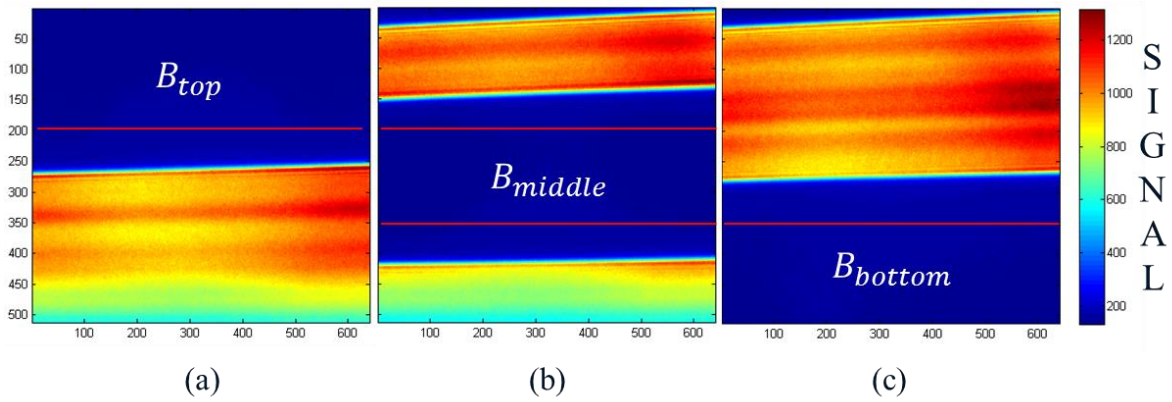

Figure 3.4: Background Creation

For Imaging Location 1, the top section was taken for the first 200 rows of the image with the top of the laser blocked. When the middle of the laser was blocked, rows 200 to 350 were cut. Similarly, for the bottom, rows 350 to 512 were extracted. Stitching all of these together, the background image is created, as shown by Equation 3.1.

$$B = B_{top} + B_{middle} + B_{bottom} \tag{3.1}$$

Looking more closely at the values of the regions that are stitched together, the average value averaged over all the columns level off to a background value that is higher than the ambient signal – this now accounts for the scatter and biased in a signal when taking and image for a temperature measurement (laser on), for example. Figure 3.5 illustrates these points. The "Best Guess Final BKD" is the stitched together image created previously and the "Avg Profile" is the full, unblocked laser sheet. This is later defined to be the average air scattering image.

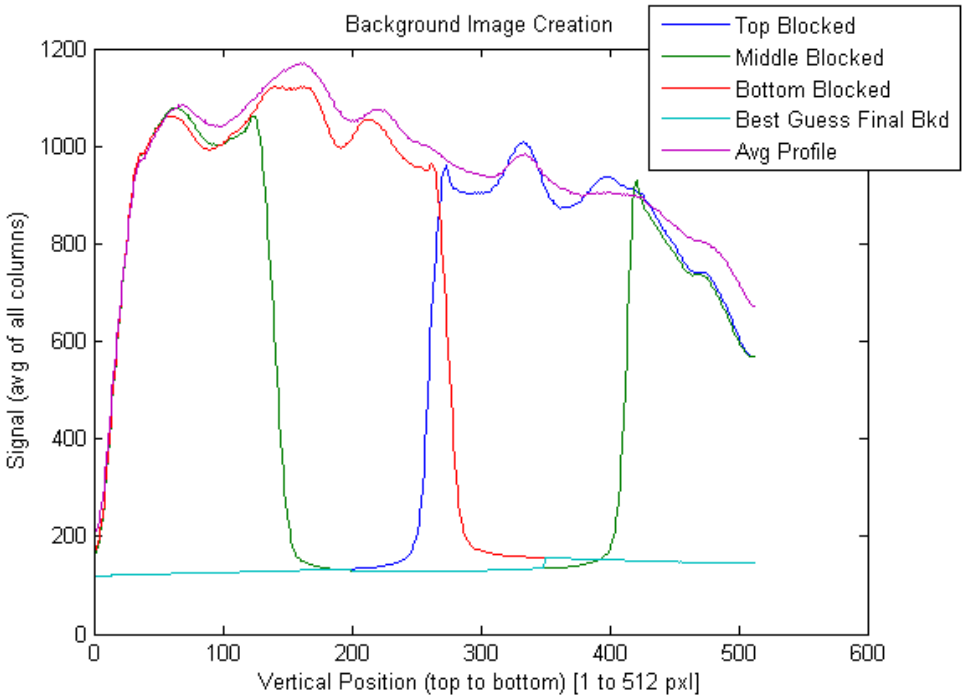

Figure 3.5: Background Image Creation

It is clear in the figure that the top and middle blocked regions level off to a similar value, while the bottom is somewhat higher. It is not exactly known why this is, but is probably caused by more laser sheet scattering from the blocker that is then captured by the camera than the top and middle regions. This is a topic that is further explored in *Chapter 4*.

In order to erase any appearance of this background image subtraction in the flame temperature image, the average value of the entire background image was used for subsequent calculations. Ideally, the stitched background image would be used; however it would result in a temperature image with horizontal lines which are figments of the temperature calculation method. The average background values for all three imaging locations are given in Table 3.1.

Table 3.1: Average Background for 3 Locations

	Location 1	Location 2	Location 3
B_{avg}	135	140	134

As shown, the average background values are very similar and reflect consistency throughout the imaging on each location. Even though a single number is being used for the background subtraction, the blocking technique provided a more accurate estimation of the background while taking measurements since an ambient background value would have been approximately 67. To put these values in perspective, the saturation limit on the camera with the given conditions and setup was 4095 counts. This will be discussed more in *Chapter 4* as well.

3.4 Room Temperature Air and Burner Flame Measurement

Next, the laser blocks are removed and the full sheet is imaged in filtered room temperature air and in the burner flame. A total of 2000 single images were collected for each situation to reduce noise then background subtracted according to Equation 3.2. The total 2000 images are separated into two variables, A_1 and A_2, each an average of 1000 single images. This is done to determine a calibration constant, which is discussed in detail in the next section.

$$M_1 = A_1 - B_{avg} \;\&\; M_2 = A_2 - B_{avg} \tag{3.2}$$

The burner flame images are done in a similar manner according to Equation 3.3, where Z is average of the single burner flame images.

$$F = Z - B_{avg} \tag{3.3}$$

Single image samples of *F* are provided in Figure 3.6.

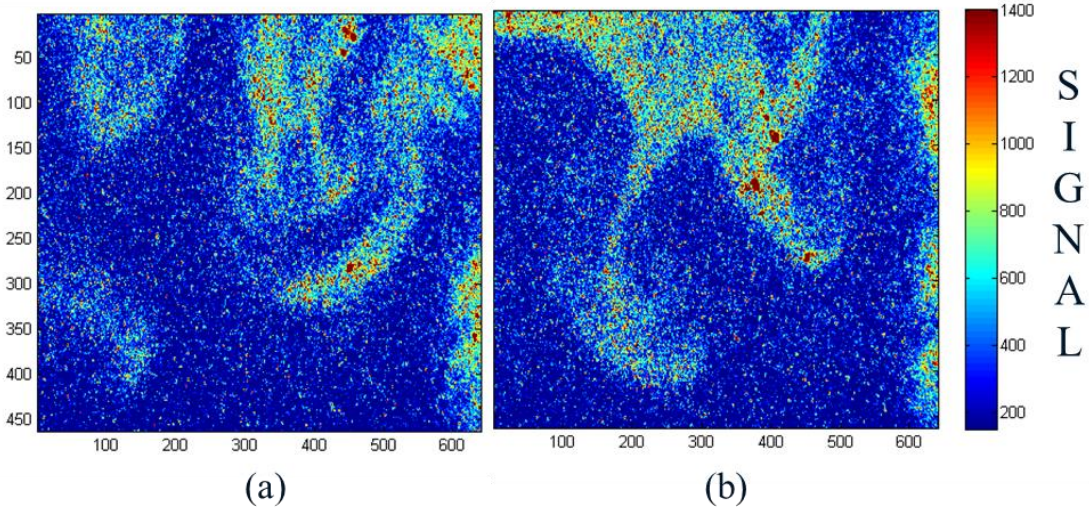

Figure 3.6: Single Images of Flame Signal

From these two sample single images of *F*, it is evident that there is often times mixing of the hot and colder gases, and can create pockets of cold gas that are even quite close to the burner surface. This is shown by the large difference in the signal. The cold regions are approximately 1000 counts and the hot regions are approximately 400 counts.

3.5 Temperature Calibration Method

After determining an appropriate background and subtracting it from the raw signal for the air and burner images, the flame temperature can be found using image processing. The calibration constant is found using Equation 3.4, where T_{RT} is 295 Kelvin.

$$C = T_{RT} M_1 \tag{3.4}$$

An image of the room temperature air scattering can then be found by Equation 3.5.

$$T_{RT} = \frac{C}{M_2} \tag{3.5}$$

The room temperature image is shown in Figure 3.7.

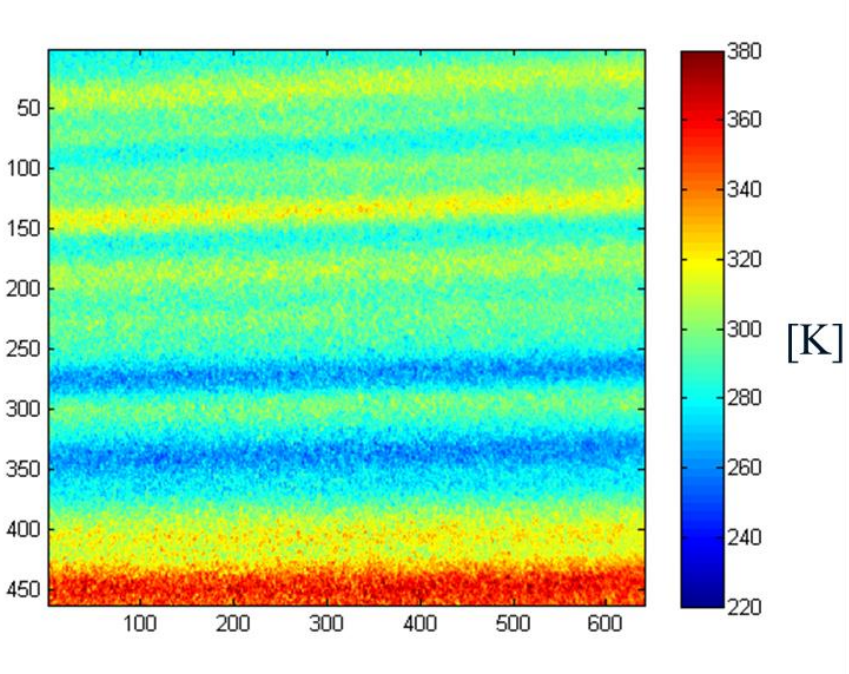

Figure 3.7: Room Temperature Image

Since room temperature was measured to be 295 K, this image would ideally be 295 at every pixel. However, due to laser sheet energy variation over time, there is a variation in room temperature in the vertical direction. The overall mean is 295 K. Finally, taking the ratio of the calibration constant, C, and F, the flame temperature of the burner can be found in Equation 3.6.

$$T_{Flame} = \frac{C}{F} \tag{3.6}$$

T_{Flame} is shown in Figure 3.8.

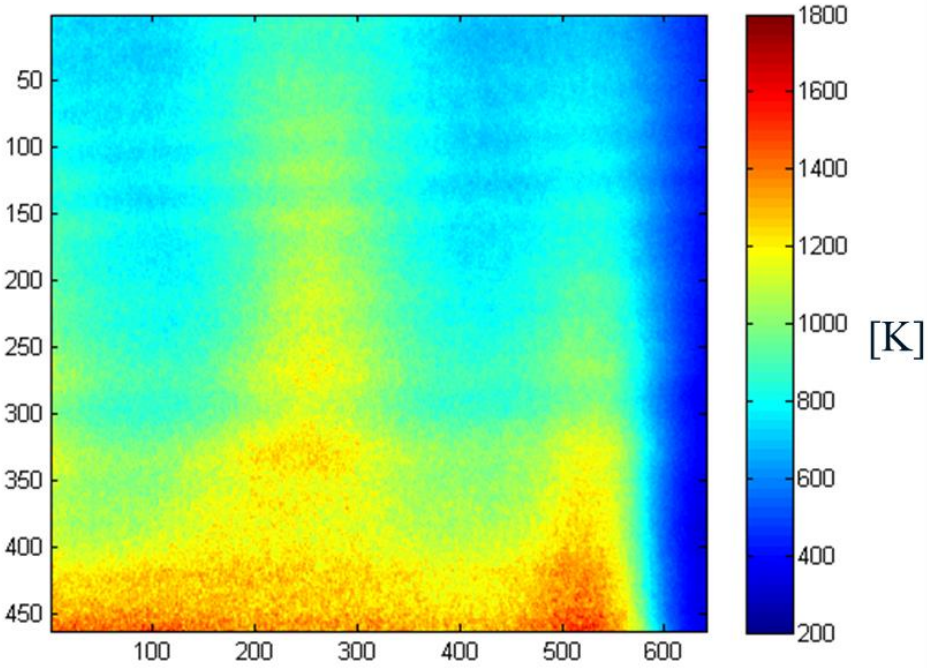

Figure 3.8: Flame Temperature – Location 1 in Figure 3.1

Inspecting this figure, one can see the cooler gas beyond column 600 shown by the blue color scale. Also, the hottest temperatures are concentrated near the surface of the burner. It is important to keep in consideration that this average flame temperature image does, in fact, not truly capture the temperature behavior of the burner. As we saw in the single image samples of *F*, pockets of cold gas are often in the hot regions of gas – even on the left side of the image, further away from the edge. In other words, a gradual change from hot to cold moving vertically upward, isn't entirely accurate as shown in the image.

CHAPTER 4

Results and Discussion

4.1 Overview of Results

With the image processing and temperature calibration process now established, the flame temperature and further analysis of the data can be performed. The average flame temperature and fluctuation in that temperature is first considered. Since average temperature images characterize a single temperature, the fluctuation or standard deviation about this average is also of interest. The uncertainty in the laser Rayleigh scattering technique temperature measurements is found to quantify the accuracy of the measurements. The adiabatic flame temperature of process is then evaluated and compared to the average temperature measurements. Thermocouple and infrared camera measurements are presented and compared to the laser Rayleigh scattering technique. Concluding, the radiant heat energy is estimated.

4.2 Average Flame Temperature and Temperature Fluctuation

The average flame temperature and flame temperature fluctuation or standard deviation is presented for each imaging location in Figure 4.1. The temperature fluctuation images were spatial averaged by a 10 by 10 pixel filter. Thus, the resolution of the temperature fluctuation images is reduced by a factor of 10 compared to the average flame temperature images. This is done to minimize noise.

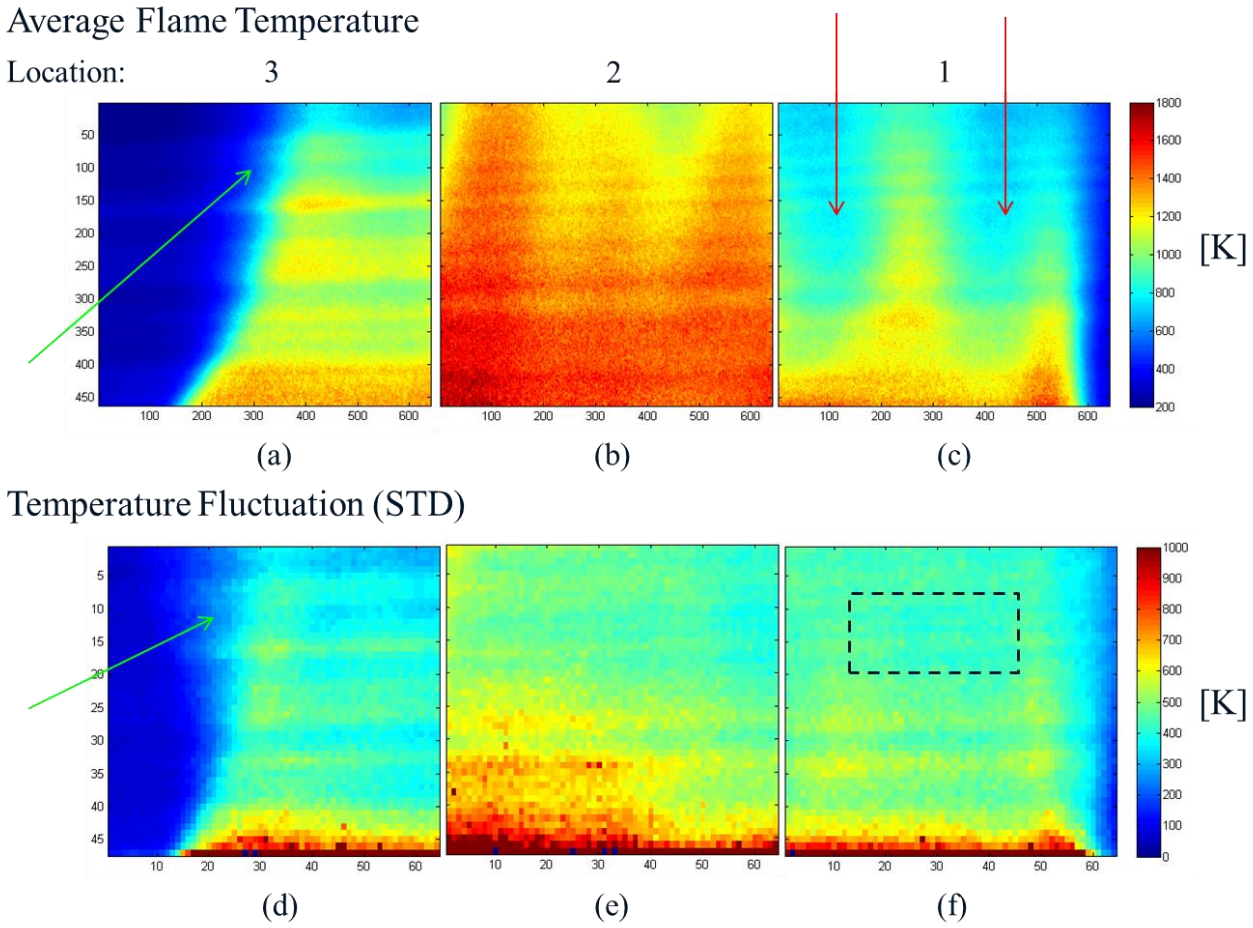

Figure 4.1: Average Flame Temperature and Temperature Fluctuation

Considering first the average flame temperature images, the flame temperature is hottest on average near the burner surface and cooler moving further vertically and away from the burner surface. Also, the regions outside the combustion zone (far left and far right) go to a temperature near room temperature. Additionally, there is some variation in the horizontal temperature across all the images. These peaks and valleys of high and low average temperature across the horizontal profile (red arrows on image c) correspond to the 6 raised ridges or "bumps" in the mesh surface of the burner – an interesting temperature property of the physical design of this burner to minimize acoustical noise. This was found by analyzing the location of

the imaging regions (Figure 3.1) and their spatial relationship to the ridges on the burner. There is also variation in the vertical temperature profile of each location, which is fictitious. These variations or striations are caused by laser sheet energy variation over time. In other words, the energy across the laser sheet varied in position, thus varying the temperature. If the spatial laser sheet energy variation was more minimal in the room temperature measurements and the burner measurements, then the vertical striations would also be greatly reduced. However, as presented in the average flame temperature images, some vertical variation remains indicating that the laser energy variation is slightly different over time in the room temperature and burner measurements. This is also noticeable in the room temperature image presented in Figure 3.7.

Considering now the fluctuation about the mean flame temperature, the fluctuation at a given position can be large (even at the top of the imaging location). These pockets of high fluctuation exist, and indicate that there is mixing of cooler and warmer gases which shows flame behavior not readily apparent from the average temperature images (dotted box on image f). The fluctuation in location 1 and 2 shows that the gas temperature is changing the most closest to the burner and decreasing as we move vertically away from the burner surface. Also, in location 3, the top left region of the image shows higher temperature fluctuation in a point where the average flame temperature is relatively low. This indicates a high mixing zone where there are hot temperature flares (green arrows on image a and d).

In order to examine the average and fluctuation or standard deviation of these temperatures more closely, four regions were defined for comparison from location 3. Table 4.1 presents the regions, along with the standard deviation and mean temperature. An average of 10 rows by 10 columns was selected to minimize noise.

Table 4.1: Selected Regions with Mean and Standard Deviation of Temperature

Region	1	2	3	4
Image Rows	150 to 159	150 to 159	150 to 159	400 to 409
Image Columns	100 to 109	200 to 209	500 to 509	500 to 509
Mean ($\bar{T}$)	307	467	1319	1387
Std. Dev. (σ)	103	279	456	536

Figure 4.2 points out directly the standard deviation and average temperature for imaging location 3 at the four regions of interest.

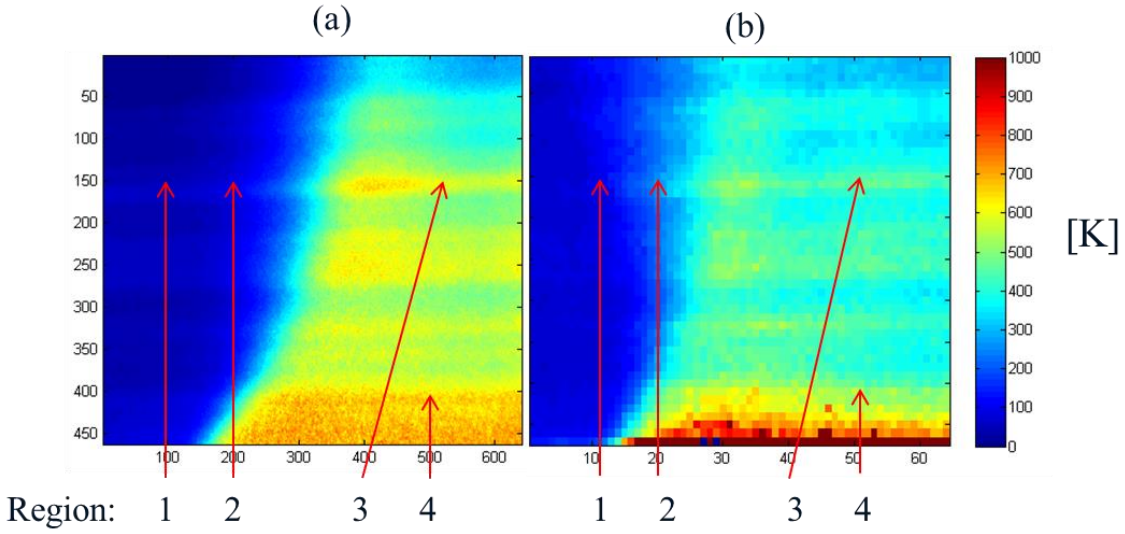

Figure 4.2: Location 3 Average Flame Temperature and Temperature Fluctuation

As the Table 4.1 and Figure 4.2 indicate, the temperature follows the average flame temperature trends presented previously – lower temperatures outside the flame zone and increasingly higher at the burner surface. From this data, it is also clear that the higher

temperature regions also have a greater standard deviation. Figure 4.3 shows the histogram for each region's 1000 image data set.

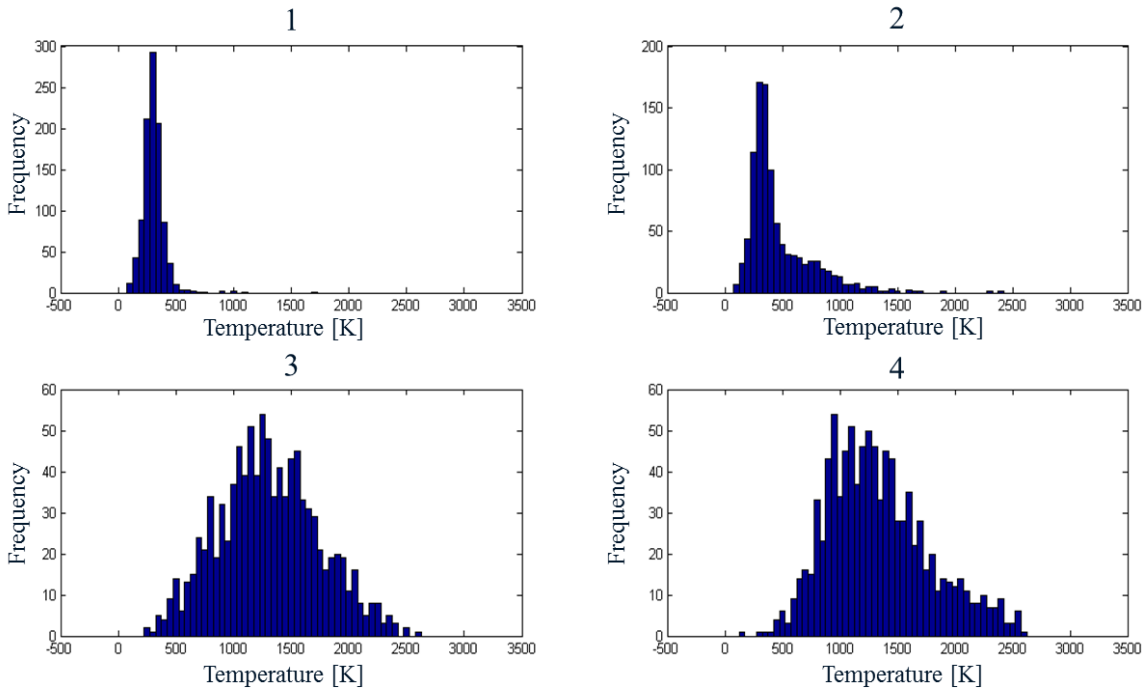

Figure 4.3: Selected Regions Complete Histogram

In this figure, it is clear where the values in Table 4.1 came from. Region 1 has an average close to room temperature, with a small fluctuation from that mean. Moving to region 2, we see the standard deviation increase as the position of interest moves closer to the edge of the flame. Then, in regions 3 and 4 the temperature increases as expected in the main combustion zone with a large increase in standard deviation. These increases in standard deviaiton can be explained by the mixing of hot and cold gases in that area as well as the amount of signal collected at high temperatures. The higher the temperature, the lower the signal and the more sensitive the temperature measurement is to uncertainty and noise which contributes to this higher standard deviation. The uncertainty in the analysis is explored in the next section.

A software filtering method was also applied to the data and determined that any effect of saturated pixels caused by Mie scattering did not alter the results measurably. This is further discussed in *APPENDIX I*.

4.3 Laser Rayleigh Scattering Technique Uncertainty Analysis

The uncertainty in the flame temperature measurement is an important consideration as well. Using Equation 3.2, 3.3, 3.4, and 3.6, the flame temperature can also be described as Equation 4.1, where all the variables are the same as previously defined.

$$T_{Flame} = \frac{T_{RT}(A_1 - B_{Avg})}{(Z - B_{Avg})} \tag{4.1}$$

Assembling the flame temperature in this manner allows for a more straightforward approach in calculating the uncertainty. From Equation 4.1, the absolute uncertainty in the flame temperature can be written as Equation 4.2.

$$\delta T_{Flame} = \pm\left[\left(\frac{\partial T_{Flame}}{\partial T_{RT}}\delta T_{RT}\right)^2 + \left(\frac{\partial T_{Flame}}{\partial A_1}\delta A_1\right)^2 + \left(\frac{\partial T_{Flame}}{\partial B_{Avg}}\delta B_{Avg}\right)^2 + \left(\frac{\partial T_{Flame}}{\partial Z}\delta Z\right)^2\right]^{\frac{1}{2}} \tag{4.2}$$

After taking the partial derivatives, simplifying, and substituting in the flame temperature equation (Equation 4.1), the overall relative uncertainty in the flame temperature is given by Equation 4.3.

$$\frac{\delta T_{Flame}}{T_{Flame}} = \pm\left[\left(\frac{\delta T_{RT}}{T_{RT}}\right)^2 + \left(\frac{\delta A_1}{A_1 - B_{Avg}}\right)^2 + \left(\frac{-\delta B_{Avg}}{A_1 - B_{Avg}}\right)^2 + \left(\frac{\delta B_{Avg}}{Z - B_{Avg}}\right)^2 + \left(\frac{-\delta Z}{Z - B_{Avg}}\right)^2\right]^{\frac{1}{2}} \tag{4.3}$$

Next, each term is evaluated. Equation 4.4 substitutes in values used in the measurement and calculates the overall relative flame temperature uncertainty in location 1.

$$\frac{\delta T_{Flame}}{T_{Flame}} = \pm\left[\left(\frac{0.7}{295}\right)^2 + \left(\frac{\sqrt{961}}{961-135}\right)^2 + \left(\frac{-\sqrt{135}}{961-135}\right)^2 + \left(\frac{\sqrt{135}}{401-135}\right)^2 + \left(\frac{-\sqrt{401}}{401-135}\right)^2\right]^{\frac{1}{2}} = \pm 0.096 \quad (4.4)$$

Looking at the magnitude of each term, the uncertainty contribution from the room temperature measurement is quite low; while the contribution from the last term is most dominate.

With the total uncertainty now found, its effect on the measured average flame temperature can now be quantified. Figure 4.4 plots the column averaged flame temperature (up until the edge of the burner) for location 1 along with the temperature profile shifted by the overall uncertainty.

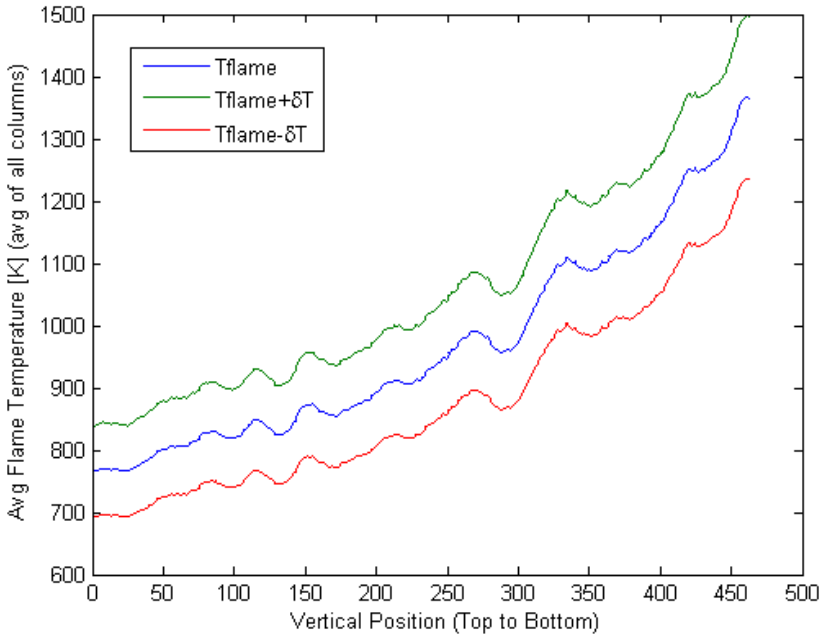

Figure 4.4: Average Flame Temperature Shifted by Uncertainty at Location 1

In this figure, we see the effect the uncertainty has on the average flame temperature measurement. At positions far from the burner (temperatures of 692 to 838 K) the effect is approximately ± 73 K, while near the surface (temperatures of 1237 to 1500 K), the effect can be

significant at approximately ± 131 K. Higher error in the high temperature regions and lower error in the low temperature regions is intuitive since there is less signal in the high temperature regions than in the low temperature ones.

Considering the blocking technique to calibrate an accurate background signal resulted in higher accuracy in the flame temperature imaging. For example, without using a blocking technique to determine the real background signal during measurements, one might have used the background signal with no laser present. The average (256 images) ambient background with no laser present was 66.7 counts. This is drastically different than the background used in this study of 135 (51 % difference) and implementing this ambient background instead would have resulted in an average flame temperature 127 K (13.8 % difference) lower on average. Using this blocking technique for a background measurement then is much more accurate than simply implementing the ambient background image or value with no laser present.

4.4 Adiabatic Flame Temperature

In order to compare the temperature results from the laser Rayleigh scattering technique with a theoretical benchmark, the constant pressure adiabatic flame temperature can be calculated. This is a measure of the maximum possible flame temperature in a complete combustion process with no heat or other energy losses. Similar to the chemical reaction equation (Equation 2.1) for this process, the enthalpy balance for methane at room temperature and the products at the adiabatic flame temperature is shown in Equation 4.5.

$$h_{CH_4} = h_{CO_2} + 2h_{H_2O} + \frac{7.52}{\varphi} h_{N_2} + (\frac{2}{\varphi} - 2)h_{O_2} \tag{4.5}$$

Based on this relation and the equivalence ratio as defined previously (φ=0.725), the adiabatic flame temperature was determined to be *1889 K*. EES source code used for the calculation of the

temperature is found in *APPENDIX IV*. Table 4.2 shows the adiabatic flame temperature for various equivalence ratios, and at the stoichiometric condition (φ=1, no excess air).

Table 4.2: Adiabatic Flame Temperatures for Various Equivalence Ratios

Equivalence Ratio (φ)	Excess Air (%)	Adiabatic Flame Temp. [K]
0.725	38	1889
0.833	20	2068
0.909	10	2188
1	0	2325

Based on this calculation, the average flame temperatures in each location fit well below this upper limit of 1889 K. As the excess air is decreased and the reaction becomes more stoichiometric, the adiabatic flame temperature increases. At stoichiometric conditions (φ=1, no excess air), the adiabatic flame temperature reaches 2325 K. By simply increasing the excess air in the reaction, the adiabatic flame temperature can be lowered. Considering an entire water heater system, providing a larger amount of air for the combustion process would effectively result in a less efficient system. While providing more excess air does lower the flame temperature ultimately, this method is still not an ideal method of NO_x reduction in water heater burner design.

4.5 Thermocouple and IR Camera Temperature Measurement

Using the experimental setup as described in *Thermocouple Measurement and IR Camera Experimental Setup*, a thermocouple measurement was made for comparison with the laser Rayleigh scattering technique. After approximately 1 minute in position and after the flame

achieved steady state operation, the thermocouple reached a steady-state value of 826°C or 1099 K via the LabVIEW software's thermocouple measurement interface. Since this is the thermocouple temperature and not the combustion gas temperature, some analysis was done to estimate the actual temperature of the combustion gases. The details can be found in *APPENDIX II*. After estimating corrections for radiation effects in competition with convective heat transfer from the gases to the thermocouple, the temperature of the combustion gases at the thermocouple location was estimated to be 1508 ± 30 K.

In comparison, the average temperature measurement by the laser Rayleigh scattering technique was found to be 1428 ± 131 K in the same location that the thermocouple was positioned, 5 cm above the center of the burner surface (image average of a 10 x 10 region). The percent difference between the two measurement techniques is then 5.6%.

The thermocouple was then moved to a position near the edge of the burner, but before a steady-state value was achieved, the thermocouple failed and forced the conclusion of testing. This result was not surprising since this temperature is at the upper limit of the thermocouple's capabilities and further illustrates the points made about the use of thermocouples for temperature measurement in combustion application as discussed in *Temperature Measurement Using a Thermocouple*. Despite these thermocouples being relatively low-cost instruments, additional thermocouples were not available. However, further testing would have likely resulted in failure as well due to the high temperatures observed. While the thermocouple measurement provided a temperature in close agreement with the laser Rayleigh scattering technique, it required much more time for a single point measurement, and the physical device in this case ultimately failed due to the high temperature.

An infrared camera was also implemented to observe the flame temperature according to the set-up previously described. Due to the high temperature in the burner flame combustion gases, this IR camera was unable to perform accurate quantitative temperature measurements but did provide some qualitative data. Figure 4.5 shows the image of the burner in operation on the left and the IR filtered image (which is smaller than the standard image) on the right with its position outlined on the left image.

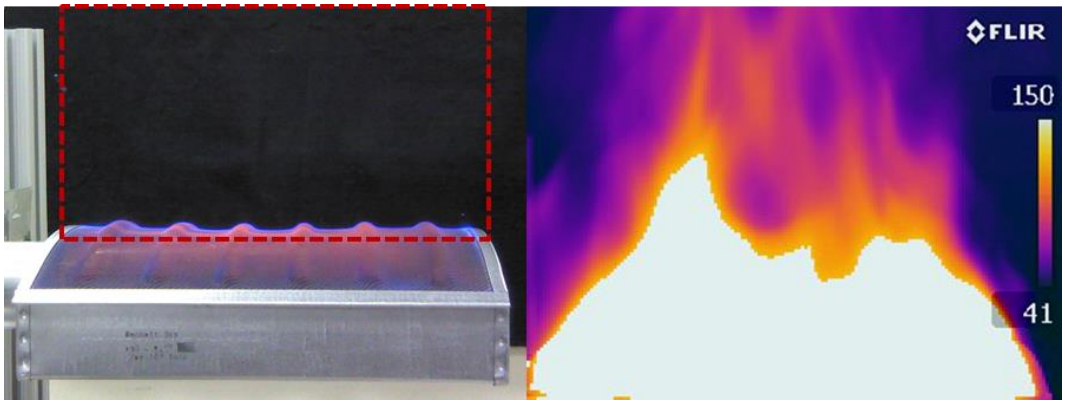

Figure 4.5: Burner Image with IR filtered image

As shown in the IR image, the flame temperature is saturated in the lower (and hottest) regions and moves out of saturation in the regions further from the surface of the burner. One is able to change the temperature range of the camera, but the change in temperature that is captured by the camera is limited to a maximum of 150°C – still very small compared to the temperature changes in this flame and burner. Additionally, the camera's temperature range was only -4 to 1202°F or 253 to 923 K so even with an adjustable range, the flame temperature present (especially near the burner surface) were often in excess of 923 K. Figure 4.6 shows the structure of the emitting gases above this burner further from the burner surface.

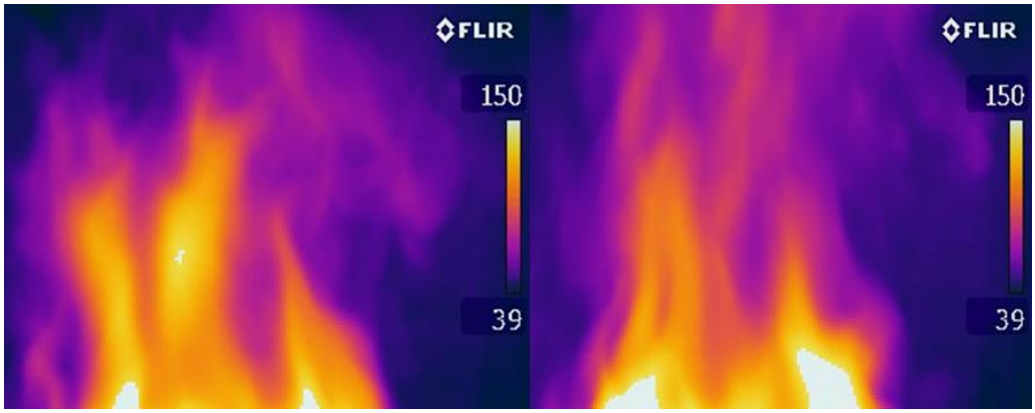

Figure 4.6: Upper Flame Structure

In these images, the flame structure shown is similar to the structure previously presented by the laser Rayleigh scattering technique. There are large pockets of colder gases that can be close to the burner surface and large fluctuations where mixing is occurring. Despite the inability of this camera to provide temperature measurements, we can see confirmation of the large scale mixing process of hot and cold gases and the fluctuation of flame structures similar to the laser Rayleigh scattering technique.

4.6 Radiant Heat Energy

Since it is known that this particular burner has significant radiative properties, the radiant heat energy or amount of energy emitted in the form of radiation is of interest. New, low- NO_x burners make use of radiation to keep combustion temperatures low and further reduce emissions. In order to quantify the radiant properties of this particular burner, the radiant heat energy and percent radiant heat energy can be found. Using the right side of Equation 4.5, the energy required for the products at the adiabatic flame temperature can be written as Equation 4.6. This assumes no conduction or other losses.

$$E_{adiabatic} = h_{CO_2} + 2h_{H_2O} + \frac{7.52}{\varphi} h_{N_2} + (\frac{2}{\varphi} - 2)h_{O_2} \quad (4.6)$$

The adiabatic energy describes the smallest amount of energy required for the reaction at the adiabatic temperature. The amount of energy required for a reaction at the thermocouple temperature and laser Rayleigh scattering temperature can also be found similarly (E_{TC} and E_{LRS}). In each case, the energy in the form of radiation ($E_{rad,loss}$) was found by taking the difference between the energy at the measured temperature by the two methods and the adiabatic energy. Thus, taking the ratio of the adiabatic energy to the radiative energy measured by the thermocouple, the fraction of energy in radiation measured by the thermocouple ($\Phi_{rad,TC}$) can be calculated. This is done in Equation 4.7.

$$\Phi_{rad,TC} = \frac{E_{adiabatic}}{E_{rad,loss}} = \frac{E_{adiabatic}}{E_{TC} - E_{adiabatic}} \frac{-74,954\,kJ/kmol}{-210,824\,kJ/kmol} = 0.356 \quad (4.7)$$

Similarly, the fraction of energy in radiation measured by the laser Rayleigh scattering technique ($\Phi_{rad,LRS}$) can be calculated (Equation 4.8).

$$\Phi_{rad,LRS} = \frac{E_{adiabatic}}{E_{rad,loss}} = \frac{E_{adiabatic}}{E_{LRS} - E_{adiabatic}} = 0.295 \quad (4.8)$$

It is shown here that an average of 32.5% of the energy produced by this burner in the reaction is radiative. Increasing this percent of radiative energy produced in future burner designs would further reduce flame temperatures. This could be accomplished perhaps by using a larger mesh surface area on the burner.

CHAPTER 5

Conclusion and Future Work

5.1 Conclusion

The goal of this study was to determine the average flame temperature of a low-NO_x water heater burner in multiple regions of interest. The average temperature images and fluctuation of the combustion gases shown in Figure 4.1 found by laser Rayleigh scattering are novel. In general, these average temperatures ranged from 800-1600 K. The uncertainty in the laser Rayleigh scattering technique temperature measurements was determined to be 9.6% or 73-131 K. The fluctuations in these temperatures ranged from 200-800 K on average and indicated the presence of large scale hot and cold gas mixing. Other key results were presented such as the adiabatic flame temperature, which was found to be 1889 K after performing the energy balance. By increasing the amount of excess air to the system to our equivalence ratio of 0.725, it was shown that the adiabatic flame temperature would be reduced by 436 K. However, providing a larger amount of air for the process would decrease the overall efficiency, and thus is not an ideal method of NO_x reduction in all cases.

The thermocouple measurement provided a comparable data point to the laser Rayleigh scattering technique. The thermocouple after some corrective calculation measured a gas temperature of 1508 ± 30 K – 5.3% difference to the laser Rayleigh scattering measurement of 1428 ± 131 K. While the IR camera did not provide quantitative temperature measurements, similar flame structure and behavior was observed to that of the laser Rayleigh scattering single images. These showed regions of cold gas pockets mixing with high temperature combustion gases. Further illustrations of this behavior were supported in the fluctuation images and

histograms at multiple small regions on the flame found by measurements from the laser Rayleigh scattering method. Finally, it was also estimated that 32.5% of the energy produced by this burner in the reaction is radiative energy. Due to this significant radiative property, the temperature of the gases was further reduced by an average of 420 K from the thermocouple and laser Rayleigh scattering measurements. Increasing this percent of radiative energy produced in future burner designs would further reduce flame temperatures.

According to the EPA, thermal NO_x, which is the primary mode of formation in this application, is formed in much smaller concentrations when temperatures are below 1300°C or 1573 K [13]. Looking more closely at the average flame temperature images found in the laser Rayleigh scattering technique; the temperature range is large, but approximately range from 800-1600 K above the burner. Additionally, the corrected thermocouple flame temperature reading was 1508 ± 30 K. Based on these measurements, we can observe that this burner operates largely under the EPA's maximum temperature for low NO_x concentration emissions.

5.2 Future Work

Based on the work in this study, there are improvements to the methods and approaches that can implemented in future work.

5.2.1 Improved Co-Flow and/or Method for Particle Filtering

A large amount of time in this study was spent developing an efficient method to provide clean air free of larger particles in the flow. Filtering the supply air for the burner and utilizing a co-flow around the burner for the entrainment of air provided the measurements with a reasonably large particle free region. Upon first testing for imaging locations 1 and 3, the region just outside the field of view, some large particles were present which would occasionally be

entrained into the flow. The entrainment resulted in spotting in the average flame temperature images due to these particles saturating the groups of pixels temporarily. Circular regions that tended to be farther from the burner surface would appear and bias the temperature measurement by up to 20% in a single image. The results presented in this work however did not indicate significant temperature bias due to this phenomenon.

Improving this set up with a larger co-flow 3-4 lengths of the burner on either side would further prevent larger particles from being entrained and allow for more measurement locations to be taken further from the burner edge or further vertically from the burner surface. Alternatively, a cleanroom could also be used or the burner could be in a duct, much like in a real water heater. Implementing a duct system could present larger challenges though. The duct would need to be optically accessible and consideration of reflections and spurious scattering would be a greater challenge potentially than with an open system and co-flow as used here.

5.2.2 Improved Analysis of Actual Background

Further work could be done studying the actual background for the measurements. While some uncertainty in the background is always expected, more effort could be spent to verify whether the background used in this study is reasonable. One could do this by blocking less of the laser sheet in the calibration method and thus stitching together more image sections to produce a final background image. The idea behind this is to avoid large jumps in the background level where each section is stitched together. Avoiding large jumps in the signal eliminates the need to find a single total average background value as done in this study and instead uses the stitched together image itself for background subtraction. If all the sections correspond to a similar minimum then there is no bias in the temperature calibration method

from the background. Also, utilizing a background image would remove spatial biases in the background, which a single value does not accomplish.

5.2.3 Reduction of Uncertainty in Temperature

Reducing the uncertainty in the temperature calculation can be a straight-forward adjustment. In this case, a higher laser power could have been used for the measurements to get more signal from the gas molecules. Approximately 50% of the available laser power was used for these measurements. Some care must be exercised however when considering what laser power to select. Since the signal from the air (low temperature) is much higher than the signal from the burner gases (high temperature), the air measurements are much more likely to saturate the camera. The laser power was selected on very conservative estimates due to the potential for large particle entrainment that was previously discussed, which would lead to camera saturation. The point still remains though that increasing the signal will reduce the effect of the uncertainty in the flame temperature calculation. A solution to this might be to use a different laser energy setting for the burner measurements and air measurements. The difference between these two energies could be found and incorporated into the calibration constant. This would ensure a lower overall uncertainty, but does assume that any energy variation in the laser sheet isn't significantly different between the two settings. The laser energy variation is the cause of the vertical striations as discussed previously.

Another consideration in making this adjustment is the background signal itself. A higher laser power will result in more signal, but could also significantly affect the background signal. A rise in background signal could be caused by more scattering from various surfaces. Additionally, when performing the blocking technique for the background, the scattering off the blocker itself can be significant and hard to control, deflect and contain so it does not reach the

camera's field of view. There is a fine balance between having a large amount of signal available, while still maintaining a relatively low background level.

REFERENCES

[1] U.S. Department of Housing and Urban Development and U.S. Department of Commerce, 2011, "American Housing Survey for the United States: 2009," Economic and Statistics Administration.

[2] AGA Residential Marketing, "Natural Gas Water Heaters," http://www.aga.org/Kc/resourcesbydiscipline/comm/prtips/Pages/NaturalGasWaterHeaters.aspx.

[3] Ryan, D., Long, R., Lauf, D., Ledbetter, M., and Reeves, A., 2010, "Water Heater Market Profile," US Department of Energy.

[4] GARD Analytics, Inc., 2001, "Impacts of Minnesota Energy Code on Residential Water Heater Installations: Energy Cost, Emissions, Safety and Electric Reliability," American Gas Association.

[5] U.S. E.P.A., 2012, "History of the Clean Air Act," http://epa.gov/air/caa/caa_history.html.

[6] U.S. E.P.A., "Nitrogen Dioxide: Basic Information," http://www.epa.gov/oar/nitrogenoxides/basic.html.

[7] Koshland, C. P., 1996, "Impacts and Control of Air Toxics from Combustion," Twenty-Sixth Symposium (International) on Combustion, 26(2), pp. 2049-2065.

[8] Bowman, C. T., 1992, "Control of combustion-generated nitrogen oxide emissions: Technology driven by regulation," Twenty-Fourth Symposium (International) on Combustion, 24(1), pp. 859–878.

[9] U.S. E.P.A., 2013, "Air Pollution Control Technology Fact Sheet," EPA.

[10] U.S. E.P.A., 1995, "Low Emissions Water Heater Burner," Reports & Assessments, http://cfpub.epa.gov/ncer_abstracts/index.cfm/fuseaction/display.abstractDetail/abstract/1483/report/0.

[11] Hunt, M. e. a., 2008, "Super-Efficient Gas Water Heating Initiative, Prepared for the California Energy Commission: Public Interest Energy Research Program."

[12] Drnevich, R., Meagher, J., Papavassiliou, V., Raybold, T., Stuttaford, P., Switzer, L., and Rosen, L., 2013, "Low NOx Emissions in a Fuel Flexible Gas Turbine," Department of Energy.

[13] U.S. E.P.A., 1999, "Nitrogen Oxides (NOx) Why and How They Are Controlled," EPA.

[14] A.O. Smith, 2012, "Low NOx Power Burner Models," http://www.hotwater.com/lit/spec/com_gas/aoscg11000.pdf.

[15] Genesys Combustion, Inc., 1992, "Flue Gas Recirculation for NOx Reduction."

[16] Eckbreth, A. C., 1996, Laser Diagnostics for Combustion Temperature and Species, CRC Press.

[17] Lückerath, R., Woyde, M., Meier, W., Stricker, W., Schnell, U., Magel, H.-C., Görres, J., Spliethoff, H., and Maier, H., 1995, "Comparison of coherent anti-Stokes Raman-scattering thermometry with thermocouple measurements and model predictions in both natural-gas and coal-dust flames," Applied Optics, 34(18), pp. 3303-3312.

[18] Laurendeau, N. M., 1988, "Temperature Measurements by Light-Scattering Methods," Progress Energy Combustion Science, 14(2), pp. 147-170.

[19] Kohse-Höinghaus, K., and Jeffries, J. B., 2002, Applied Combustion Diagnostics, CRC Press.

[20] Hecht, E., 2002, Optics, Pearson Addison Wesley.

[21] Miles, R. B., Lempert, W. R., and Forkey, J. N., 2001, "Laser Rayleigh scattering," Measurement Science and Technology, 12(5).

[22] Hecht, J., 1994, Understanding Lasers: An Entry-Level Guide, IEEE Press, New York.

[23] Su, L. K., Helmer, D. B., and Brownell, C. J., 2010, "Quantitative planar imaging of turbulent buoyant jet mixing," Journal of Fluid Mechanics, 643, pp. 59-95.

[24] Incropera, F., DeWitt, D., Bergman, T., and Lavine, A., 2007, Fundamentals of Heat and Mass Transfer, Wiley.

[25] Nellis, G., and Klein, S., 2009, Heat Transfer, Cambridge University Press.

APPENDIX I – Software Filtering

A software filtering method was explored as well in this study due to the concern of Mie scattering caused by large dust particles in the field of view which would lead to camera saturation. The software filtering code counted the number of saturated pixels in an image and replaced it with the value of NaN (not a number). Table AI.1 displays the results of the average number of saturated pixels in a single image.

Table AI.1: Average Number of Saturated Pixels in a Single Image

Location	3	2	1
Air, A_1	128	105	85
Air, A_2	140	115	80
Burner, Z	897	7	139

As shown here, the number of saturated pixels can vary somewhat based on location and the type of data collected (air or burner measurements). We can conclude here though that the order of these values is in the 10s or 100s or 1000s. Considering that the number of pixels in a single image is 512 x 640, or 327,680, the number of saturated pixels is relatively small. This means that even if there are 1000 saturated pixels on average, 0.3 % of the data is so erroneous that the signal exceeds the saturation limit. With this small amount of effect from the Mie scattering and saturated pixels in a single image does not translate into a significant change in the average flame temperature or fluctuation. Much of this result can be contributed to the setup of an air filter system and co-flow system to provide dust free air around the burner for measurements. Without these systems, the Mie scattering contribution to the signals would have been much more significant.

APPENDIX II – Thermocouple Temperature Correction

In order to achieve a more accurate thermocouple measurement of the gas temperature, a model of the energy exchange between the burner and the thermocouple was created. A diagram of this is shown in Figure AII.1.

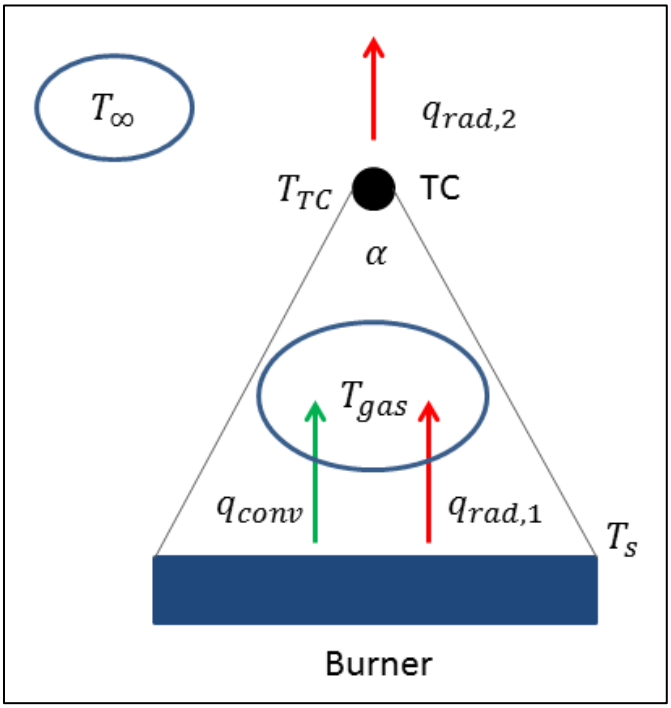

Figure AII.1: Thermocouple Temperature Correction Energy Exchange Model

As shown in the figure, there are two radiation terms and a convection term. T_∞ is the temperature of the ambient room, T_s is the temperature of the burner surface, and T_{gas} is the temperature of the combustion gases. Conservation of energy at the thermocouple requires that the sum of the energy transfer terms equals zero under steady state conditions. This is Equation AII.1.

$$q_{conv} + q_{rad,b\ to\ TC(1)} - q_{rad,TC\ to\ \infty(2)} = 0 \qquad \text{(AII.1)}$$

Each term in this equation is then defined by Equation AII.2 and AII.3.

$$q_{conv} = hA_{TC}(T_s - T_{TC}) \quad \text{(AII.2)}$$

$$q_{rad,b\ to\ TC} = \sigma A_b \varepsilon_b \varepsilon_{TC} \hat{F}_{b,TC}\left({T_s}^4 - {T_{TC}}^4\right) \ \&\ q_{rad,TC\ to\ \infty} = \sigma A_{TC} \varepsilon_\infty \varepsilon_{TC} \hat{F}_{TC,\infty}\left({T_{TC}}^4 - {T_\infty}^4\right) \quad \text{(AII.3)}$$

Since the temperature of the burner surface is not well known, thermodynamic equilibrium was assumed between the burner surface and the temperature of the gas as shown in Equation AII.4.

$$T_{gas} = T_s \quad \text{(AII.4)}$$

Assembling the term then in Equation AII.1 leads to Equation AII.5.

$$hA_{TC}(T_{gas} - T_{TC}) = \sigma[-A_b \varepsilon_b \varepsilon_{TC} \hat{F}_{b,TC}\left({T_{gas}}^4 - {T_{TC}}^4\right) + A_{TC} \varepsilon_\infty \varepsilon_{TC} \hat{F}_{TC,\infty}\left({T_{TC}}^4 - {T_\infty}^4\right)] \quad \text{(AII.5)}$$

Before solving this equation, a few parameters need to be established since the heat transfer coefficient, *h*, must be found. The burner surface was modeled as a flat, rectangular surface (10 in x 7.5 in). The emissivity of the burner, ε_b, was approximated to be 0.9 and the emissivity of the thermocouple, ε_{TC}, was approximated to be 0.8 based on their material composition. Thermal and fluid properties for Nitrogen at 1300 K were used since they are the majority of the molecules in the gas flow. The Prandtl number is then found in Equation AII.6

$$Pr = \frac{c_p \mu}{k} = 0.70 \quad \text{(AII.6)}$$

Since the volumetric flow rates are known, the area of the burner can then be used to find the velocity of the flow. Equation AII.7 determines the local Reynolds number (based on diameter) with the volumetric flow rate corrected due to heating (approximately half).

$$Re_D = \frac{\rho v D}{\mu} = 0.92 \quad \text{(AII.7)}$$

Based on this Reynolds number, Incropera lists a Nusselt number correlation and coefficients for a cylinder in cross flow (similar to the given situation) given by Equations AII.8 and AII.9 [24].

$$C = 0.911\ and\ m = 0.385 \quad \text{(AII.8)}$$

$$Nu = C{Re_D}^m Pr^{1/3} = 0.78 \quad \text{(AII.9)}$$

Using the Nusselt number, thermal conductivity of Nitrogen, and the diameter of the thermocouple, the heat transfer coefficient can be found by Equation AII.10.

$$h = \frac{Nu \cdot k}{D_{TC}} = 19.2 \ \frac{W}{m^2 K} \tag{AII.10}$$

Lastly, a view factor for the radiation from the burner surface to the thermocouple and radiation from the surroundings to the thermocouple is considered. The view factor is defined as the fraction of radiation from one surface to another. At each surface, the view factor to the other two surfaces and to itself was found by finding the fraction of the solid angle and using the reciprocity relation [24]. Additionally, since each surface had multiple view factors to the respective temperature sources, Equation AII.11 was used to simplify and estimate an effective view factor for the heat transfer model in Equation AII.5 [25].

$$\hat{F}_{i,j} = F_{i,j} + \sum_{k=1}^{N}(1 - \varepsilon_k)F_{i,k}\hat{F}_{k,j} \ for \ i = 1..N \ and \ j = 1..N \tag{AII.11}$$

Using this relationship, the effective view factor ($\hat{F}_{i,j}$) was found to be $1.53x10^{-4}$ for the radiation term from the burner to the thermocouple ($\hat{F}_{b,TC}$) and 0.6135 for the term from the thermocouple to the surroundings ($\hat{F}_{TC,\infty}$). Finally, going back to Equation AII.5 and plugging in the known values, the actual temperature of the combustion gases can be found, $T_{gas} = 1508$ K.

Since the emissivity of the thermocouple and burner surface is not exactly known, there is some uncertainty in this gas temperature. Other sources of uncertainty are found in the simplification of the energy model and the assumption that the gas temperature is in thermodynamic equilibrium with the burner surface (Equation AII.4). Also, at the Reynold's number found, a laminar flow would be concluded, but the heat transfer is likely turbulent in the actual flow. With the emissivities of the burner surface and thermocouple varied by a conservative 15%, the temperature of the gas varied by ± 30 K. This can be used as an overall

estimate of all the uncertainties. So, the temperature of the combustion gases can then be reported as 1508 ± 30 K, keeping in mind this is a rough uncertainty approximation.

Furthermore, the gas temperature of 1508 K is higher than the laser Rayleigh scattering measurement of 1428 K in the same location as the thermocouple. This could indicate that the emissivities used in this gas temperature calculation could be smaller than estimated in this analysis. However, it more likely that this 80 K difference is due to the uncertainty in the laser Rayleigh scattering method, which had uncertainties up to 140 K in the hotter temperature regions.

APPENDIX III – Selected Matlab Image Processing Code

```
%FLUCTUATION IMAGE GENERATION

% addpath('C:\Users\3859smithn\Desktop\Research\Test
Images\SecondBurner\RS2;');
% addpath('C:\Users\3859smithn\Desktop\Research\Test
Images\SecondBurner\RS2\Air;');
% addpath('C:\Users\3859smithn\Desktop\Research\Test
Images\SecondBurner\RS2\Burner;');

for i=1:1000 % CHANGE
    if i > 999;
        name=strcat('air_',num2str(i),'.asc');
    end
    if i > 99 && i < 1000;
        name=strcat('air_0',num2str(i),'.asc');
    end
    if i > 9 && i < 100;
        name=strcat('air_00',num2str(i),'.asc');
    end
    if i < 10;
        name=strcat('air_000',num2str(i),'.asc');
    end
fid = fopen(name,'r+');
m = fscanf(fid, '%d %d', [640 512]);
fclose(fid);
img=m'; clear m fid ans name;

bksize = 10;  %Size
fun = @(block_struct) mean2(block_struct.data); %*
ones(size(block_struct.data));
redimg(:,:,i) = blockproc(img,[bksize bksize],fun);

if i == 333 || i == 666
    disp(i)
end

end

clear i fun bksize img;

%*****************************************

BkdAct = 134; RT=295;

temp = (RT .* (airimg-BkdAct)) ./ (burnerimg-BkdAct);

tempstd = std(temp(6:52,:,:),0,3);

imagesc(tempstd,[0 1000])
```

```
% INITIAL MASTER AVERAGE IMAGE GENERATION

%clc;

% addpath('C:\Users\3859smithn\Desktop\Research\Test
Images\SecondBurner\RS2;');
% addpath('C:\Users\3859smithn\Desktop\Research\Test
Images\SecondBurner\RS2\Air;');
% addpath('C:\Users\3859smithn\Desktop\Research\Test
Images\SecondBurner\RS2\Burner;');

% %Focus
sh1 = fopen('C:\Users\3859smithn\Desktop\Research\Test
Images\SecondBurner\RS2\focus.asc','r+');
shoneR = fscanf(sh1, '%d %d', [640 512]);
fclose(sh1);
focus=shoneR';
figure(1);imagesc(focus)

%*****************************************************************
%Air Scattering
%USE FOR IM1

airstart1=1; airend1=1000;
airone = zeros(512,640); numsatpxls = zeros(50,1);
airscatIm1 = zeros(512,640);
air1 = zeros(512,640); count=0;

%Measurement 1 (1000 images)
for i=airstart1:airend1
    if i > 999;
        name=strcat('air_',num2str(i),'.asc');
    end
    if i > 99 && i < 1000;
        name=strcat('air_0',num2str(i),'.asc');
    end
    if i > 9 && i < 100;
        name=strcat('air_00',num2str(i),'.asc');
    end
    if i < 10;
        name=strcat('air_000',num2str(i),'.asc');
    end
fid = fopen(name,'r+');
m = fscanf(fid, '%d %d', [640 512]);
fclose(fid);
img=m'; clear m fid ans name; index=50*count;

airone(:,:,i-index)=img;%removedust(img,4095,4);
numsatpxls(i-index,1)=countsat(img,4095);
clear img;

if i==50;
 air1 = nanmean(airone,3);
 airscatIm1 = air1; clear air1;
```

```
 avgnumsatpxls1=mean(numsatpxls);
 totavgnumsatpxls=avgnumsatpxls1;
 numsatpxls = zeros(50,1); clear avgnumsatpxls1;
 airone = zeros(512,640);
 count = count + 1;
 disp(count)
end

if i==100 || i==150 || i==200 || i==250 || i==300 || i==350 ...
    || i==400 || i==450 || i==500 || i==550 || i==600 ...
    || i==650 || i==700 || i==750 || i==800 || i==850 ...
    || i==900 || i==950 || i==1000;
 air2 = nanmean(airone,3);
 airscatIm1 = cat(3,airscatIm1,air2); clear air2;
 avgnumsatpxls2=mean(numsatpxls);
 totavgnumsatpxls=cat(2,totavgnumsatpxls,avgnumsatpxls2);
 numsatpxls = zeros(50,1); clear avgnumsatpxls2;
 airone = zeros(512,640);
 count = count + 1;
 disp(count)
end
end
clear airend1 airone airstart1 count i numsatpxls;

totalsatpxlsIm1noSF=mean(totavgnumsatpxls);

Im1noSF=nanmean(airscatIm1,3);

figure(2);imagesc(Im1noSF)
clear airscatIm1 index totavgnumsatpxls

%**************************************

%Air Scattering
%%USE FOR IM2

airstart2=1000; airend2=2000;
airone = zeros(512,640); numsatpxls = zeros(50,1);
airscatIm2 = zeros(512,640);
air1 = zeros(512,640); count=0;

%Measurement 1 (1000 images)
for i=airstart2:airend2
    if i > 999;
        name=strcat('air_',num2str(i),'.asc');
    end
fid = fopen(name,'r+');
m = fscanf(fid, '%d %d', [640 512]);
fclose(fid);
img=m'; clear m fid ans name; index=999+50*count;

airone(:,:,i-index)=img; %removedust(img,4095,4);
numsatpxls(i-index,1)=countsat(img,4095);
clear img;
```

```
if i==1050;
 air1 = nanmean(airone,3);
 airscatIm2 = air1; clear air1;
 avgnumsatpxls1=mean(numsatpxls);
 totavgnumsatpxls=avgnumsatpxls1;
 numsatpxls = zeros(50,1); clear avgnumsatpxls1;
 airone = zeros(512,640);
 count = count + 1;
 disp(count)
end

if i==1100 || i==1150 || i==1200 || i==1250 || i==1300 || i==1350 ...
    || i==1400 || i==1450 || i==1500 || i==1550 || i==1600 ...
    || i==1650 || i==1700 || i==1750 || i==1800 || i==1850 ...
    || i==1900 || i==1950 || i==2000;
 air2 = nanmean(airone,3);
 airscatIm2 = cat(3,airscatIm2,air2); clear air2;
 avgnumsatpxls2=mean(numsatpxls);
 totavgnumsatpxls=cat(2,totavgnumsatpxls,avgnumsatpxls2);
 numsatpxls = zeros(50,1); clear avgnumsatpxls2;
 airone = zeros(512,640);
 count = count + 1;
 disp(count)
end
end

clear airend2 airone airstart2 count i numsatpxls;

totalsatpxlsIm2noSF=mean(totavgnumsatpxls);

Im2noSF=nanmean(airscatIm2,3);

figure(2);imagesc(Im2noSF)
clear airscatIm2 index totavgnumsatpxls


%*********************************************************************

%Build Bkd Img

bkdstart=1; bkdend=8;

%Background Middle
for i=bkdstart:bkdend
name=strcat('bkdmid_000',num2str(i),'.asc');
fid = fopen(name,'r+');
m = fscanf(fid, '%d %d', [640 512]);
fclose(fid);
bkdmid(i,:,:)=m';
end

%Background Bottom
for i=bkdstart:bkdend
name=strcat('bkdbot_000',num2str(i),'.asc');
fid = fopen(name,'r+');
```

```
m = fscanf(fid, '%d %d', [640 512]);
fclose(fid);
bkdbot(i,:,:)=m';
end

%Background Top
for i=bkdstart:bkdend
name=strcat('bkdtop_000',num2str(i),'.asc');
fid = fopen(name,'r+');
m = fscanf(fid, '%d %d', [640 512]);
fclose(fid);
bkdtop(i,:,:)=m';
end

bkdmidavg = squeeze(mean(bkdmid,1));
bkdbotavg = squeeze(mean(bkdbot,1));
bkdtopavg = squeeze(mean(bkdtop,1));

figure(4);imagesc(bkdmidavg);
figure(5);imagesc(bkdbotavg);
figure(6);imagesc(bkdtopavg);

clear ans bkdbot bkdmid bkdtop fid i m name bkdstart bkdend

%****************************************************************

%Build BKD

bkdtop = bkdtopavg(1:199,:);

bkdmiddle = bkdmidavg(200:349,:);

bkdbottom = bkdbotavg(350:512,:);

BKD = [bkdtop; bkdmiddle; bkdbottom];

figure(7);imagesc(BKD);

clear bkdbottom bkdmiddle bkdtop

%****************************************************************

%Build BKD Plot

TopSec = bkdtopavg;
TopSecAvg = mean(TopSec,2);

MidSec = bkdmidavg;
MidSecAvg = mean(MidSec,2);

BotSec = bkdbotavg;
BotSecAvg = mean(BotSec,2);
```

```
Im1Avg = mean(Im1noSF,2);

BKDAvg = mean(BKD,2);

BKDAct = mean(BKDAvg)

x = 1:512;
figure(8);
plot(x,TopSecAvg, x, MidSecAvg, x, BotSecAvg, x, BKDAvg,x, Im1Avg)
title('Background Image Creation');
xlabel('Vertical Position (top to bottom) [1 to 512 pxl]');
ylabel('Signal (avg of all columns)');

hleg = legend('Top Blocked','Middle Blocked','Bottom Blocked','Best Guess
Final Bkd','Total Profile (Im1)');

clear TopSec TopSecAvg MidSec MidSecAvg BotSec BotSecAvg Im1Avg BKDAvg hleg x
%
%*********************************************************************

%Burner Scattering - Flame Images (1-2000)

imstartflame=1; imendflame=2000;
postflameimg = zeros(512,640); numsatpxls = zeros(50,1);
burnerscat = zeros(512,640);
air1 = zeros(512,640); count=0;

%Measurement 1 (1000 images)
for i=imstartflame:imendflame
    if i > 999;
        name=strcat('burner_',num2str(i),'.asc');
    end
    if i > 99 && i < 1000;
        name=strcat('burner_0',num2str(i),'.asc');
    end
    if i > 9 && i < 100;
        name=strcat('burner_00',num2str(i),'.asc');
    end
    if i < 10;
        name=strcat('burner_000',num2str(i),'.asc');
    end
fid = fopen(name,'r+');
m = fscanf(fid, '%d %d', [640 512]);
fclose(fid);
img=m'; clear m fid ans name; index=50*count;

postflameimg(:,:,i-index)=img; %removedust(img,4095,4);
numsatpxls(i-index,1)=countsat(img,4095);
clear img;

if i==50;
 air1 = nanmean(postflameimg,3);
 burnerscat = air1; clear air1;
 avgnumsatpxls1=mean(numsatpxls);
 totavgnumsatpxls=avgnumsatpxls1;
```

```
 numsatpxls = zeros(50,1); clear avgnumsatpxls1;
 postflameimg = zeros(512,640);
 count = count + 1;
 disp(count)
end

if i==100 || i==150 || i==200 || i==250 || i==300 || i==350 ...
    || i==400 || i==450 || i==500 || i==550 || i==600 ...
    || i==650 || i==700 || i==750 || i==800 || i==850 ...
    || i==900 || i==950 || i==1000 || i==1050 ...
    || i==1100 || i==1150 || i==1200 || i==1250 || i==1300 || i==1350 ...
    || i==1400 || i==1450 || i==1500 || i==1550 || i==1600 ...
    || i==1650 || i==1700 || i==1750 || i==1800 || i==1850 ...
    || i==1900 || i==1950 || i==2000;
 air2 = nanmean(postflameimg,3);
 burnerscat = cat(3,burnerscat,air2); clear air2;
 avgnumsatpxls2=mean(numsatpxls);
 totavgnumsatpxls=cat(2,totavgnumsatpxls,avgnumsatpxls2);
 numsatpxls = zeros(50,1); clear avgnumsatpxls2;
 postflameimg = zeros(512,640);
 count = count + 1;
 disp(count)
end
end
clear imstartflame imendflame postflameimg count i index numsatpxls;

totalsatpxlsBurner=mean(totavgnumsatpxls);

FlameAvg=nanmean(burnerscat,3);
figure(8);imagesc(FlameAvg)

FlameSignal= FlameAvg - BKDAct;
figure(9);imagesc(FlameSignal);

clear burnerscat totavgnumsatpxls

%*********************************************************************

%Temp Calibration Method

AvgImOne=Im1noSF-BKDAct; FlameSignal=FlameAvg-BKDAct;
AvgImTwo=Im2noSF-BKDAct;

RT = 295;

C = RT .* AvgImOne;

T_rt = C ./ AvgImTwo;

T_flame = C ./ FlameSignal;
%
% figure(10);imagesc(T_flame,[200,1800]);%colorbar

%*********************************************************************
```

```
%Single Shots

sh4 = fopen('C:\Users\3859smithn\Desktop\Research\Test
Images\SecondBurner\RS2\Burner\burner_0245.asc','r+');
sh4R = fscanf(sh4, '%d %d', [640 512]);
fclose(sh4);
AirSS245=sh4R';
figure;imagesc(AirSS245(50:512,:),[150,1400])
```

APPENDIX IV – EES Adiabatic Flame Calculation Code

```
"Adiabatic Flame Temperature Calculation"

"Governing chemical reaction - Energy balance:

CH4 + 2/phi (O2 + 3.76 N2) ---> 2 H2O + 1 CO2 + (7.52/phi) N2 + (2/phi -2) O2"

"Equivalence Ratio Calc:"

"excessair=0.20

excessair=1/phi-1"

"COE for Const P Burn:"

phi=0.725

hch4=2*hH2O + hCO2 + 7.52/phi*hN2 + (2/phi-2)*hO2

"EOS for Enthalpies:"

hch4=enthalpy(CH4, T=21.85)

hH2O=enthalpy(H2O, T=Taft)

hCO2=enthalpy(CO2,T=Taft)

hN2=enthalpy(N2,T=Taft)

hO2=enthalpy(O2,T=Taft)

hN21=enthalpy(N2,T=21.85)

HCO21=enthalpy(CO2,T=21.85)
```